

Electronic supplementary information (ESI)

***In situ*-polymerized lithium salt as a polymer electrolyte for high-safety lithium metal batteries**

Shenghang Zhang^{a,b,c,h}, Fu Sun^a, Xiaofan Du^a, Xiaohu Zhang^a, Lang Huang^a, Jun Ma^a, Shanmu Dong^{a,i}, André Hilger^d, Ingo Manke^d, Longshan Li^a, Bin Xie^a, Jiedong Li^a, Zhiwei Hu^e, Alexander C. Komarek^e, Hong-Ji Lin^f, Chang-Yang Kuo^{f,g}, Chien-Te Chen^f, Pengxian Han^a, Gaojie Xu^{a,b,c,i*}, Zili Cui^{a,b,c*}, Guanglei Cui^{a,b,c,h,i*}

^aQingdao Industrial Energy Storage Research Institute, Qingdao Institute of Bioenergy and Bioprocess Technology, Chinese Academy of Sciences, No. 189 Songling Road, Qingdao 266101, China.

^bShandong Energy Institute, Qingdao 266101, China.

^cQingdao New Energy Shandong Laboratory, Qingdao 266101, China.

^dHelmholtz-Zentrum Berlin für Materialien und Energie, Hahn-Meitner-Platz 1, 14109 Berlin, Germany

^eMax Planck Institute for Chemical Physics of Solids, Dresden, Germany

^fNational Synchrotron Radiation Research Center, Hsinchu, Taiwan 30076, Republic of China

^gDepartment of Electrophysics, National Yang Ming Chiao Tung University, Hsinchu 30010, Taiwan, Republic of China

^hSchool of Future Technology, University of Chinese Academy of Sciences, Beijing 100049, China

ⁱCenter of Materials Science and Optoelectronics Engineering, University of Chinese Academy of Sciences, Beijing 100049, China

*Correspondence to: xugj@qibebt.ac.cn, cuizl@qibebt.ac.cn, cuigl@qibebt.ac.cn

Experimental section

1. Electrolyte and electrode preparation

Ethyl methyl carbonate (EMC), fluoroethylene carbonate (FEC) and ethylene carbonate (EC) were all purchased from Macklin (99%) and pretreated with molecular sieves to control the H₂O content below 30 ppm. Lithium hexafluorophosphate (LiPF₆) was purchased from Aladdin. LiFPA salt was successfully synthesized according to our previous work.¹ The baseline electrolyte was 1 M LiPF₆ EMC/FEC (1:1 by volume). 1 M LiFPA EMC/FEC (1:1 by volume) was prepared by dissolving LiFPA into EMC and FEC mixed solvents. 3D-SIPE-LiFPA was obtained by heating 1 M LiFPA EMC/FEC (1:1 by volume) at 60 °C for 12 hours. The absolute content of EMC/FEC solvents in the 3D-SIPE-LiFPA is 63.8 wt.% and the solid content is 37.2 wt.%. The preparation of electrolytes was conducted in a glove box filled with argon gas (oxygen and water contents below 0.1 ppm). The water content of as-formulate electrolytes was determined at 298.15 K by Karl Fischer titration (WKT-A9).

Li metal foils (50 μm and 300 μm) were commercially available from China Energy Lithium Co., Ltd. LiNi_{0.8}Co_{0.1}Mn_{0.1}O₂ cathodes (NCM811, 18.1 mg cm⁻², 97.8 wt.% NCM811) were self-prepared. High voltage LiCoO₂ cathodes (11.0 mg cm⁻², 96.4 wt.% LiCoO₂) were purchased from Guangdong Canrd New Energy Technology Co., Ltd. For coin-type cells, the cathodes were punched into disks with a diameter of 12 mm and dried under vacuum for 12 h at 80 °C. The housing of the customized tomography cell (tomo-cell), the polyamide-imide (Torlon), was purchased from Drake plastics Europe and Bang Der plastics China.

2. Battery assembling and testing

In the Ar-filled glove box, Li/Cu, Li/Li, stainless steel/stainless steel, NCM811/Li and LiCoO₂/Li coin-type (2032) cells were assembled using glass fiber (GF-A) separator and different electrolytes (50 μL). The NCM811/Li (3.7 mAh cm⁻², 50 μm Li) pouch cells with laminated structure were assembled in a dry room (dew point < -60 °C) using a polyethylene (PE) separator (see detailed information in Table S6). The tomo-cells (see Fig. S23) were assembled with NCM811 cathode (2 mm in diameter), Li anode (2.5 mm in diameter, 300 μm thick), 100 μL electrolyte, glass fiber (GF-D,

3 mm in diameter) separator and Celgard 2325 separator (3 mm in diameter). The charge and discharge testing of cells were carried out using a LAND (Wuhan LAND electronics Co., Ltd. (China)) system. All coin-type NCM811 (3.7 mAh cm⁻², 210 mAh g⁻¹)/Li (50 μm) cells were pre-cycled at 0.2 C (1 C = 210 mA g⁻¹) for 2 cycles at room temperature. At room temperature, 50 °C and 90 °C, coin-type NCM811/Li cells (2.8-4.3 V or 2.8-4.4 V, with a constant potential charging step) were charged/discharged at 0.2 C/0.3 C for cycle life evaluation. At 0 °C, coin-type NCM811/Li cells (2.8-4.3 V, with a constant potential charging step) were directly charged and discharged at 0.1 C. At -15 °C, coin-type NCM811/Li cells (3.0-4.3 V, with a constant potential charging step) were directly charged and discharged at 0.1 C. The NCM811/Li pouch cells (2.8-4.3 V, with a constant potential charging step) were vacuum sealed after 1 formation cycle at 0.2 C, and then were charged/discharged at 0.2 C/0.3 C for cycle life evaluation. Coin-type LiCoO₂/Li (3 V-4.45 V, 1.9 mAh cm⁻², 180 mAh g⁻¹; 3 V-4.6 V, 2.2 mAh cm⁻², 210 mAh g⁻¹) were also tested. At room temperature, the NCM811/Li tomo-cells (2.8-4.3 V, with a constant potential charging step) were pre-cycled at 0.2 C for 2 cycles, then charged/discharged at 0.2 C/0.3 C upon cycling. For Li/Cu cells of modified Aurbach's measurement, first, plated 5 mAh cm⁻² Li on Cu and charged until 1 V at 0.5 mA cm⁻². Second, plated 5 mAh cm⁻² Li at 0.5 mA cm⁻² on Cu again. Third, charged to 1 mAh cm⁻² at 0.5 mA cm⁻² and then discharged to 1 mAh cm⁻² at 0.5 mA cm⁻² for 10 cycles. Last, charged to 1V at 0.5 mA cm⁻². As for the Li deposition test, Li was electrodeposited on Cu at a current density of 0.5 mA cm⁻² at a capacity of 3 mAh cm⁻². The current density/areal capacity of symmetric Li/Li was 0.5 mA cm⁻²/1 mAh cm⁻² and 1 mA cm⁻²/3 mAh cm⁻². The CE from modified Aurbach's measurement was calculated by a designed protocol:²

$$CE = \frac{Q_3 + Q_4}{Q_1 + Q_2}$$

where Q1, Q2, Q3, and Q4 represents the first plated Li capacity on Cu, the plated Li capacity in galvanostatic cycling, the stripped Li capacity in galvanostatic cycling, and the last stripped Li capacity form Cu, respectively. The measurement method of activation energy related to Li⁺ diffusion through SEI layer in Li/Li symmetrical cells is described in previous reports.³ The electrochemical impedance spectroscopy (EIS) and chronoamperometry (CA) were carried out

using the BioLogic VMP-300 workstation. Ionic conductivity (σ) was calculated according to the equation:

$$\sigma = \frac{L}{A \times R}$$

where L and A was thickness and area of the separator, respectively, while the total bulk resistance R was obtained from EIS (frequency range: 7 MHz to 100 mHz; amplitude: 10 mV) of stainless steel/stainless steel symmetric cells. The Li^+ transference number (t_{Li^+}) was examined by combination of CA and EIS in a symmetric Li/ Li cell and calculated by the following Bruce-Vincent's equation:

$$t_{\text{Li}^+} = \frac{I_s (\Delta V - I_o R_o)}{I_o (\Delta V - I_s R_s)}$$

where ΔV is the applied polarization voltage (10 mV), where I_o and I_s are the initial and steady-state current values, respectively, while R_o and R_s correspond to the resistance of the cell before and after polarization, respectively. The linear sweep voltammetry (LSV) test was also carried out on the BioLogic VMP-300 workstation.

3. Characterizations

The dry polymer powder was obtained from 3D-SIPE-LiFPA. Firstly, the as-constructed 3D-SIPE-LiFPA was washed five times with tetrahydrofuran (THF). Then, the obtained wet polymer was continuously vacuumed until it was completely dry. The successful preparation of 3D-SIPE-LiFPA was analyzed by Nuclear Magnetic Resonance Spectra (NMR, Bruker AV400 spectrometer, acetonitrile-d3). The surface morphology and elements distribution of the dry polymer powder were characterized by field emission scanning electron microscopy (SEM, Hitachi S-4800) and energy-dispersive X-ray spectroscopy (EDS). The surface chemistry of the dry polymer powder was detected X-ray photoelectron spectroscopy (XPS, Thermo Scientific ESCA Lab 250Xi), and time-of-flight secondary ion mass spectrometry (ToF-SIMS, PHI nanoTOF II). The Bruker-AXS Microdiffractometer (D8 Advance, Cu Ka radiation ($\lambda=1.5406 \text{ \AA}$)) was using to identify X-ray diffraction pattern (XRD) of the dry polymer powder.

To unveil the solvation structure of the 3D-SIPE-LiFPA, Fourier transform infrared

spectroscopy (FTIR, NICOLET 6700), Raman spectra (Microscope DXR), NMR and diffusion ordered spectroscopy NMR (DOSY NMR, Bruker AV III 500wb spectrometer.) were conducted.

Accelerating rate calorimetry (ARC, HEL-BTC500, England) was used to study the thermal runaway features of 2.8 Ah 437 Wh kg⁻¹ 100% SOC NCM811/Li pouch cell. Accelerating rate calorimetry (ARC, HEL-BTC130, England) was used to study the thermal stability of 100% SOC NCM811 cathode + electrolyte (abbreviated as cathode + electrolyte, 80 mg cathode + 500 µL electrolyte) and 100% SOC Li anode + electrolyte (abbreviated as anode + electrolyte, 80 mg anode + 500 µL electrolyte). Here, typical heat-wait-search (HWS) mode was adopted for ARC testing: one heating step was 5 °C; detection limit was 0.03 °C min⁻¹; the temperature was raised from 40 °C to 250 °C. The thermal runaway criteria was 1 °C min⁻¹. Differential scanning calorimeter (DSC, Netzsch DSC214 system) was conducted to study the thermal stability of 100% SOC NCM811 cathode (original wet state without adding additional electrolyte) and 100% SOC Li anode (original wet state without adding additional electrolyte). The heating rate of DSC test is 5 °C min⁻¹ in Ar atmosphere (50 ml min⁻¹) from 30 °C to 500 °C.

Synchrotron X-ray tomography measurement: The tomography cells (tomo-cells, after 10 cycles at discharged state) were measured at P05 beamline at DESY, Hamburg, Germany. For this measurement, the synchrotron beam energy was monochromatized to 25 KeV using a double multilayer monochromator (DMM). A CdWO₄ single crystal scintillator of 100 µm thickness was used to convert the X-ray to visible light. We used a fast KIT CMOS camera (5120 × 3840 pixels), which was kept out of the direct beam by using a mirror. 2400 projections within a 180° battery rotation were recorded with the exposure time of 25 ms. The field of view (FOV) was 3.28 × 2.46 mm², with a pixel size of 0.65 µm. Note that a binning process of 2 by 2 was used when reconstructing the dataset to get a high signal to noise ratio, yielding a spatial resolution of 1.3 µm. The tomo-cells (at the first fully charged state and after 50 cycles at discharged state) were measured at the BAMline at BESSY II, Berlin, Germany. The energy of the synchrotron beam was monochromatized to 20 KeV using a double monochromator. The detector system was comprised of a 60 µm thick CdWO₄ scintillator, a microscopic optic and a fast sCMOS camera (PCO edge 5.5) equipped with a 2560×2160 pixels CCD chip that was kept out of the direct beam by using a mirror.

A detector system with 0.6 μm pixel was used and the FOV was 3.28 x 2.46 mm^2 (width x height). 2400 projections within a 180° battery rotation were recorded with the exposure time of 20 ms. In addition, a 2 by 2 binning process was adopted when reconstructing the datasets. Therefore, the final spatial resolution was about 1.2 μm . The raw tomography data from DESY and BESSY II were processed using in-house reconstruction software programmed in IDL 8.2. First, the data was normalized and de-noised, and filtered in some cases. Then, the filtered back projection was used for final reconstruction. The reconstruction data was processed applying in-house algorithms programmed in ImageJ. The 3D demonstrations shown in the context and the supporting information were generated using Avizo.

The cycled coin-type NCM811/Li cells were disassembled in a glove box filled with argon gas. The cycled Li anode and NCM811 cathode were washed with EMC solvent. The chemical compositions of the electrode/electrolyte interphase were analyzed by using depth-profiling XPS and ToF-SIMS. To further identify some key chemical compositions (such as LiH) of cycled Li anode (unrinsed state), the *on-line* D₂O titration gas analysis mass spectrometer (MS, HPR-20, Hiden Analytical Ltd.) was performed (Fig. 5e). The morphology of the Li anodes and NCM811 cathode were characterized by SEM. The powder XRD pattern of the NCM811 cathode was collected with a Bruker-AXS Microdiffractometer. The high-resolution transmission electron microscopy (HRTEM) of NCM811 cathodes was also obtained (JEM-2100PLUS). ICP-MS (Agilent 7800) was adopted to test the transition metal ions dissolution. Soft XAS of pristine and cycled NCM811 cathodes was performed at the 11A beam-line at the National Synchrotron Radiation Research Center (NSRRC) in Taiwan. The soft XAS spectra of O *K*-edges were measured in the bulk-sensitive TFY mode, while the soft XAS spectra of Ni-*L*, Co-*L*, and Mn-*L* edges were obtained using the surface-sensitive TEY mode. To calibrate the energy scale, LiNiO₂, Li₂MnO₃, Li₂Co₂O₄, and NiO single crystals were measured for the O-*K* edges in TFY mode. Meanwhile, the NiO and LiNiO₂ single crystals were measured for the Ni-*L* edges in TEY mode. The CoO and Li₂Co₂O₄ single crystals were measured for the Co-*L* edges in TEY mode. The MnO and Li₂MnO₃ single crystals were measured for the Mn-*L* edges in TEY mode.

4. DFT calculation

All calculations (HOMO, LUMO, and bond-breaking energy) were carried out using the Gaussian 16 software. The B3LYP functional was adopted for all calculations. For geometry optimization calculations, the 6-311G(d) basis set was used. The singlet point energy calculations were performed using a larger basis set def2-TZVP basis set. The SMD implicit solvation model was used to account for the solvation effect of EMC/FEC ($\epsilon=56.48$). The DFT-D3 dispersion correction with BJ-damping was applied to correct the weak interaction to improve the calculation accuracy.

5. MD simulations

Molecular dynamic (MD) simulations of different electrolyte (EMC/FEC/LiFPA and EMC/FEC/LiPF₆) were performed to reveal the solvation structures. First, the optimized electrolyte molecules were packed in a periodic box to construct the bulk systems, the compositions of the simulated electrolytes are given in Table S5. The molar ratio between the solvent and salt used in our simulations was 5/7/1. The simulation cells contained 520 molecules. Subsequently, all mixture systems were equilibrated by NPT (i.e., isothermalisobaric) MD simulations for 5 ns at 303K and atmospheric pressure, followed by NVT (i.e., isothermal) MD simulations for 10 ns with a 1 fs time step. All MD simulations were performed using the Forcite code with Universal force field.⁴ The temperature was controlled by a Nose-Hoover Langevin (NHL) thermostat and the pressure was controlled by a Berendsen barostat.^{5,6} The Ewald scheme^{7,8} and atom-based cutoff method (i.e., a radius of 15.5 Å) were applied to treat the electrostatic and van der Waals (vdW) interactions, respectively. All the partial atomic charges were defined using the Universal force field.

Results and discussion

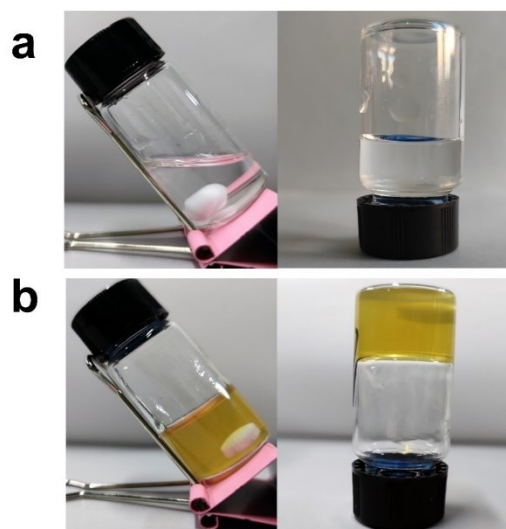


Fig. S1 | Optical images of (a) liquid state electrolyte (1 M LiFPA EMC: FEC = 1:1, by volume) and (b) as-constructed 3D-SIPE-LiFPA after thermal-induced polymerization at 60 °C for 12 hours.

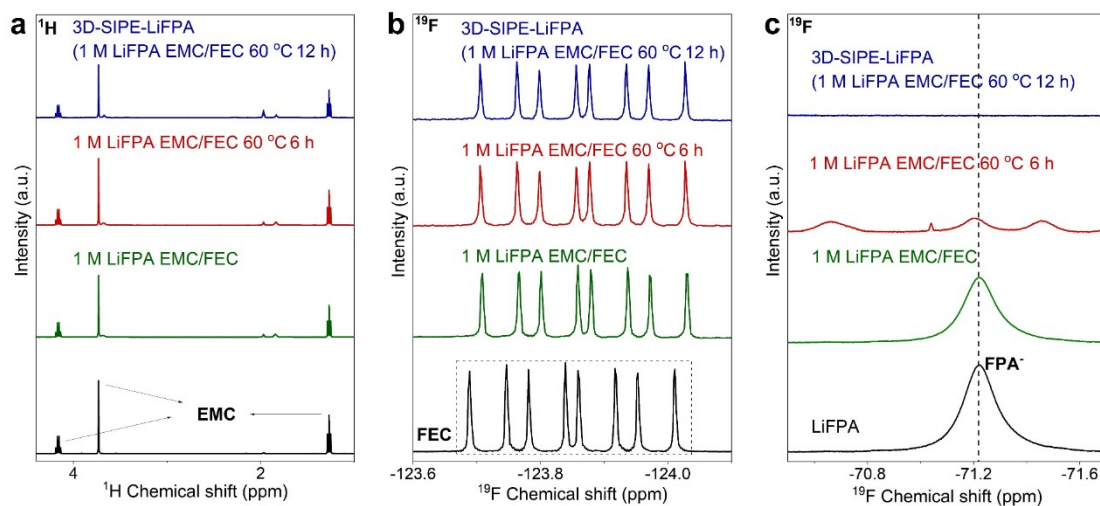


Fig. S2 | (a) ^1H NMR spectra of pure EMC and the liquid electrolyte after different heating time. (b) ^{19}F NMR spectra (from -123.6 ppm to -124.1 ppm) of pure FEC and the liquid electrolyte after different heating time. (c) ^{19}F NMR spectra (from -70.5 ppm to -71.7 ppm) of LiFPA and the liquid electrolyte after different heating time. Deuterium agent is acetonitrile- d_3 .

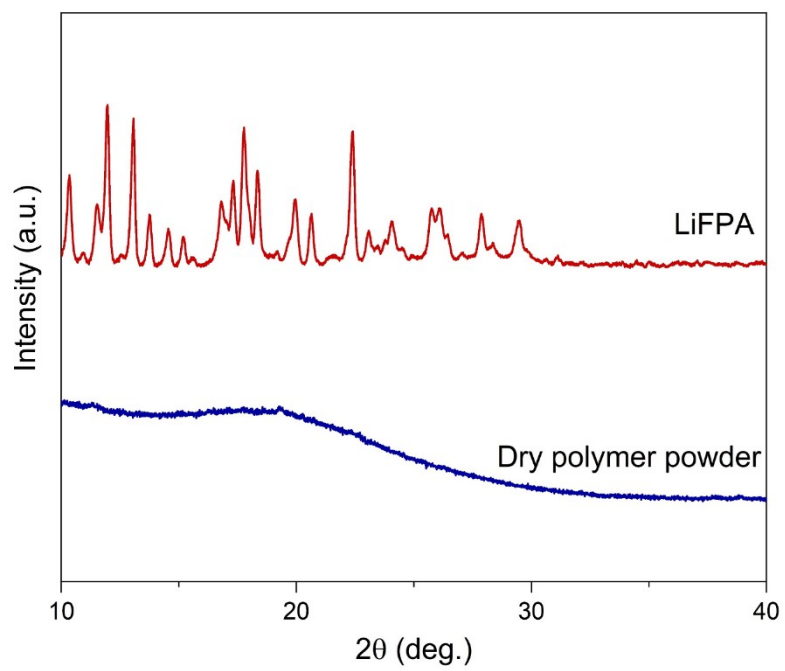


Fig. S3 | XRD patterns of LiFPA salt powder and dry polymer powder obtained from 3D-SIPE-LiFPA.

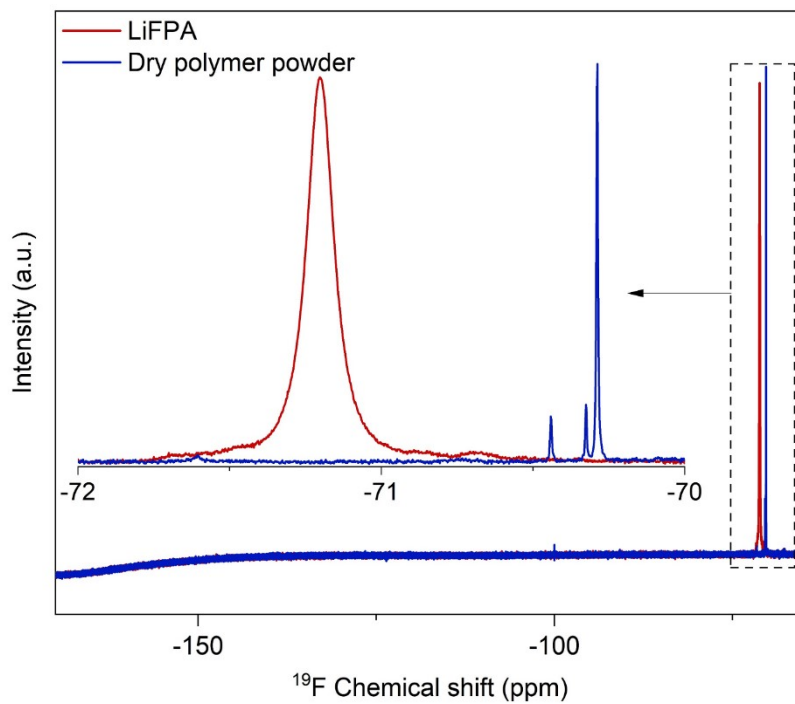


Fig. S4 | ^{19}F NMR of LiFPA salt powder and dry polymer powder obtained from 3D-SIPE-LiFPA. Deuterium agent is acetonitrile- d_3 .

In ^{19}F NMR spectra, chemical shift of $-\text{CF}_3$ in dry polymer powder and LiFPA salt is also different, locating at -70.29 ppm and -71.22 ppm, respectively.

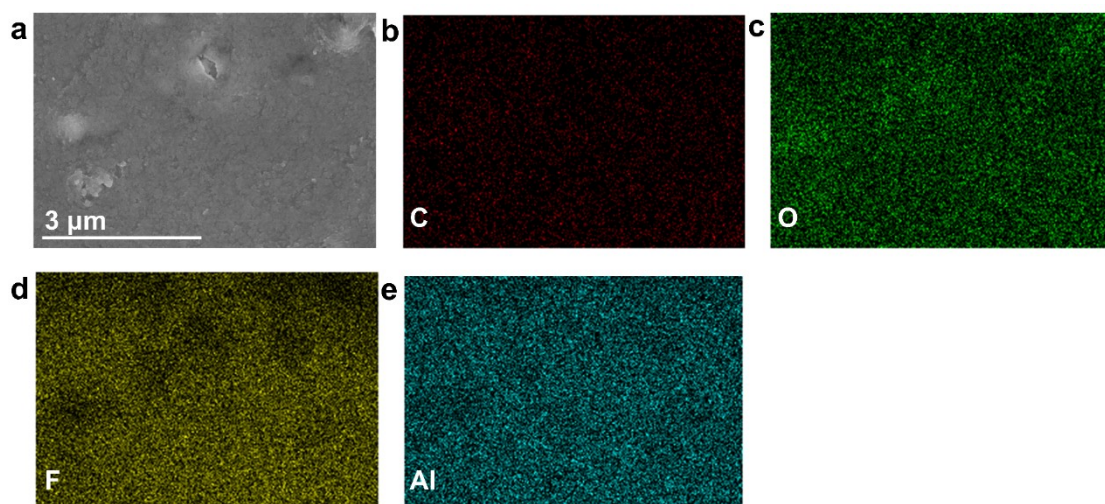


Fig. S5 | (a) The SEM image of dry polymer powder obtained from 3D-SIPE-LIFPA, and corresponding EDS mapping of (b) C element, (c) O element, (d) F element, and (e) Al element.

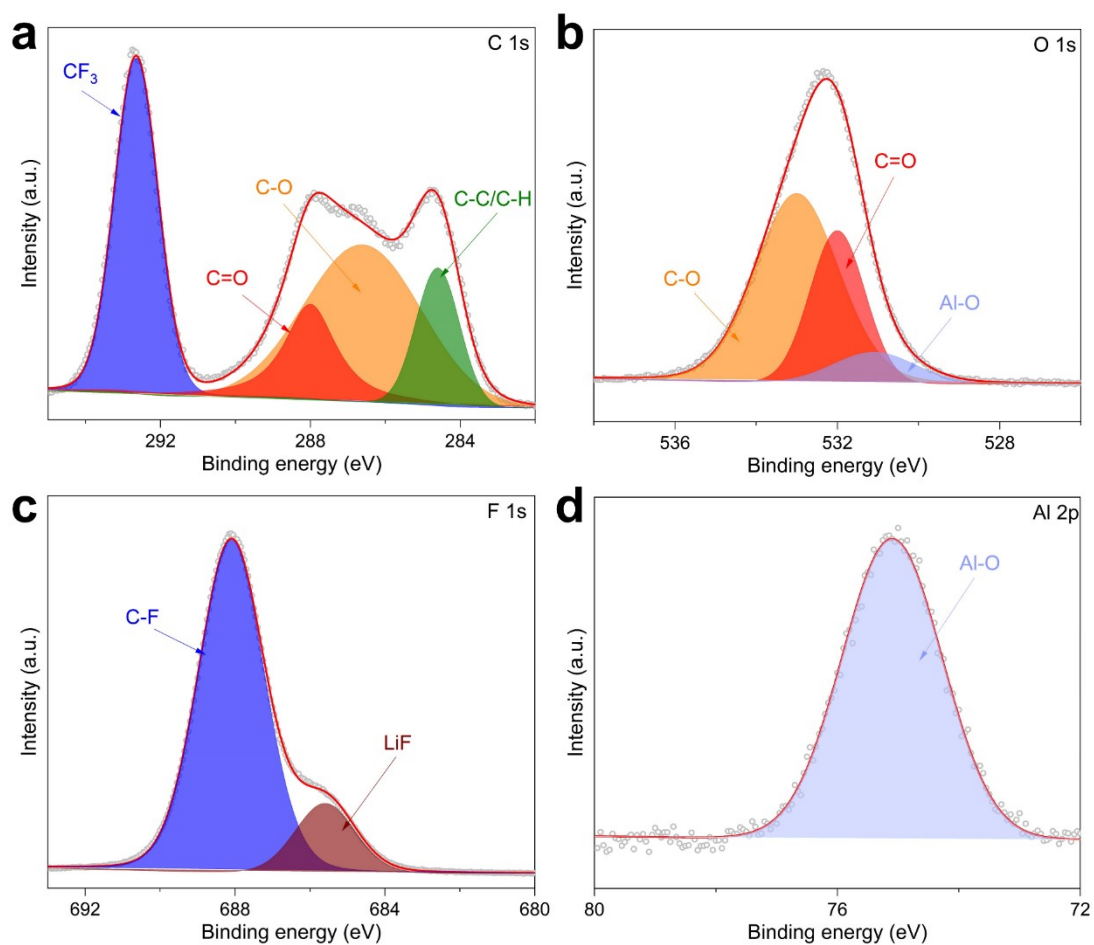


Fig. S6 | (a) C 1s, (b) O 1s, (c) F 1s, and (d) Al 2p XPS of dry polymer powder obtained from 3D-SIPE-LiFPA.

The existence of species in dry polymer powder, e.g., C-O (C1s, ca. 286.6 eV, **Fig. S6a**); O1s, ca. 533.0 eV, **Fig. S6b**), C-C (C1s, ca. 284.8 eV, **Fig. S6a**), C-F (F1s, ca. 688.5 eV, **Fig. S6c**), LiF (F 1s, ca. 685.3 eV, **Fig. S6c**), Al-O (Al 2p, ca. 75.5 eV, **Fig. S6d**), etc., are corroborated by their characteristic XPS peaks.

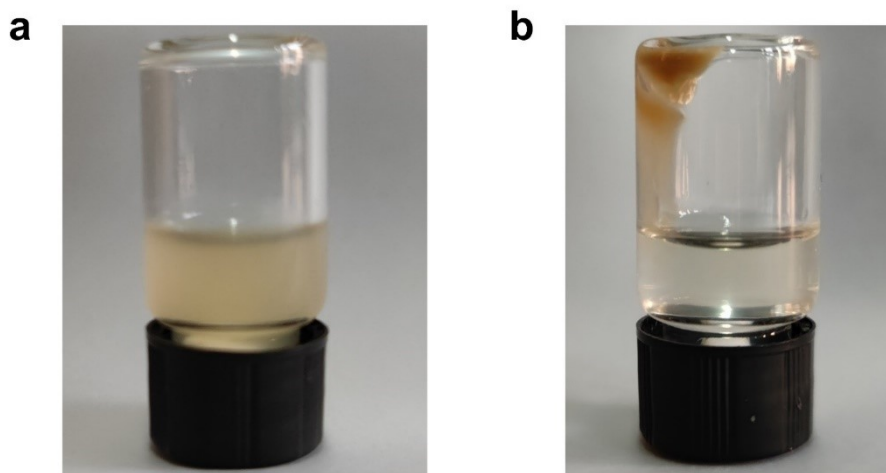


Fig. S7 | (a) The dispersed dry polymer powder in THF. (b) The centrifuged polymer.

The obtained dry polymer powder can be dispersed in THF but can hardly be dissolved, suggesting the dry polymer is 3D cross-linked.

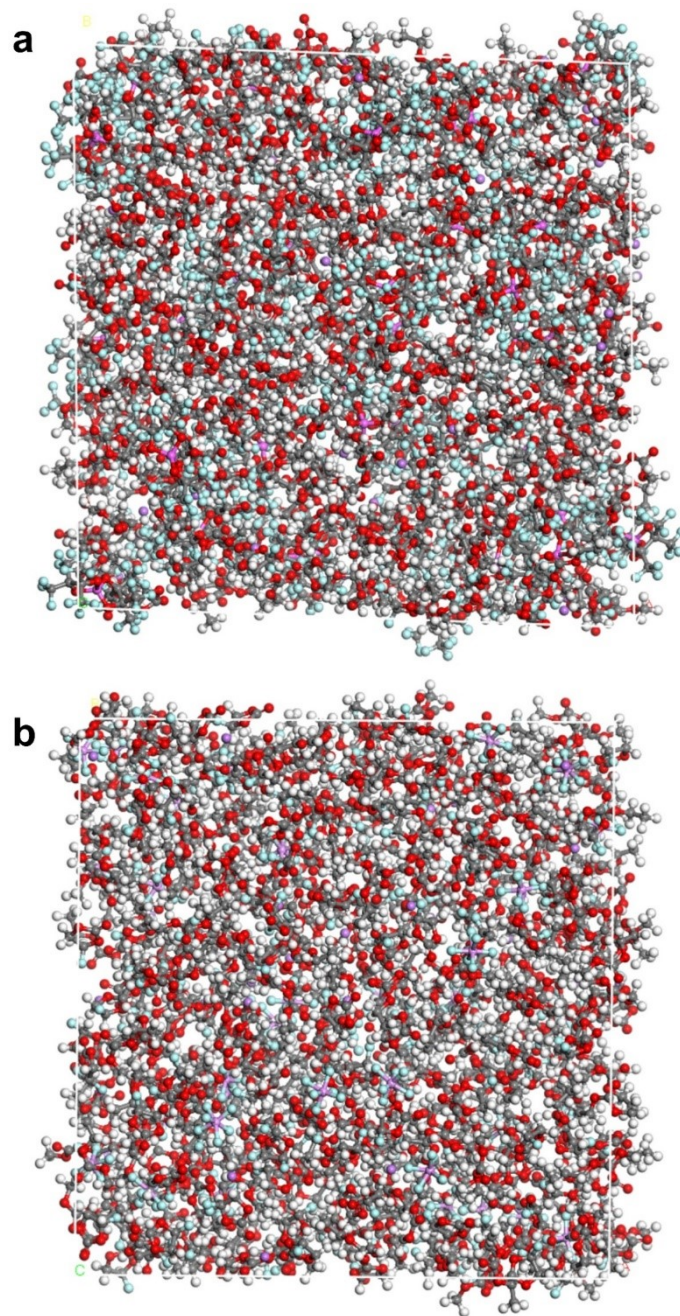


Fig. S8 | MD simulation snapshots of (a) 1 M LiFPA EMC/FEC and (b) 1 M LiPF₆ EMC/FEC. Blue balls: F atoms; red balls: O atoms; black balls: C atoms; white balls: H atoms; pink balls: Al/P atoms.

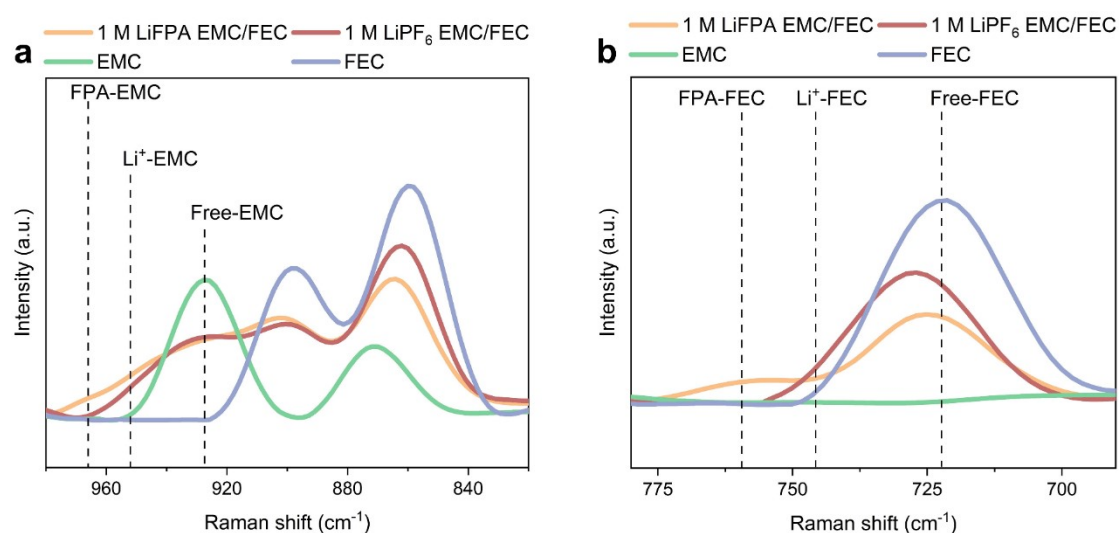


Fig. S9 | Raman spectra of 1 M LiFPA EMC/FEC electrolyte, 1 M LiPF₆ EMC/FEC electrolyte, EMC solvent, and FEC solvent from (a) 980 cm⁻¹ to 820 cm⁻¹ and (b) 780 cm⁻¹ to 690 cm⁻¹.

In Raman spectra, the peaks of 933 cm⁻¹ and 723 cm⁻¹ are related to EMC (O-C-O bending band)^{9,10} and FEC (O-C-O ring breathing mode)^{9,11}, respectively, which can be used to identify the free solvents and coordination of solvents with ions. As shown in **Fig. S9**, the Raman spectra of 1 M LiFPA EMC/FEC electrolyte, 1 M LiPF₆ EMC/FEC electrolyte, EMC solvent, and FEC solvent are added (no signal is detected in 3D-SIPE-LiFPA). Obviously, different from the free EMC (933 cm⁻¹), free FEC (723 cm⁻¹), Li⁺-EMC (950 cm⁻¹), and Li⁺-FEC (745 cm⁻¹) peaks, distinctive novel peaks centering at 966 cm⁻¹ and 759 cm⁻¹ may be ascribed to coordination of EMC-FPA (EMC-Al) and FEC-FPA (FEC-Al), respectively.

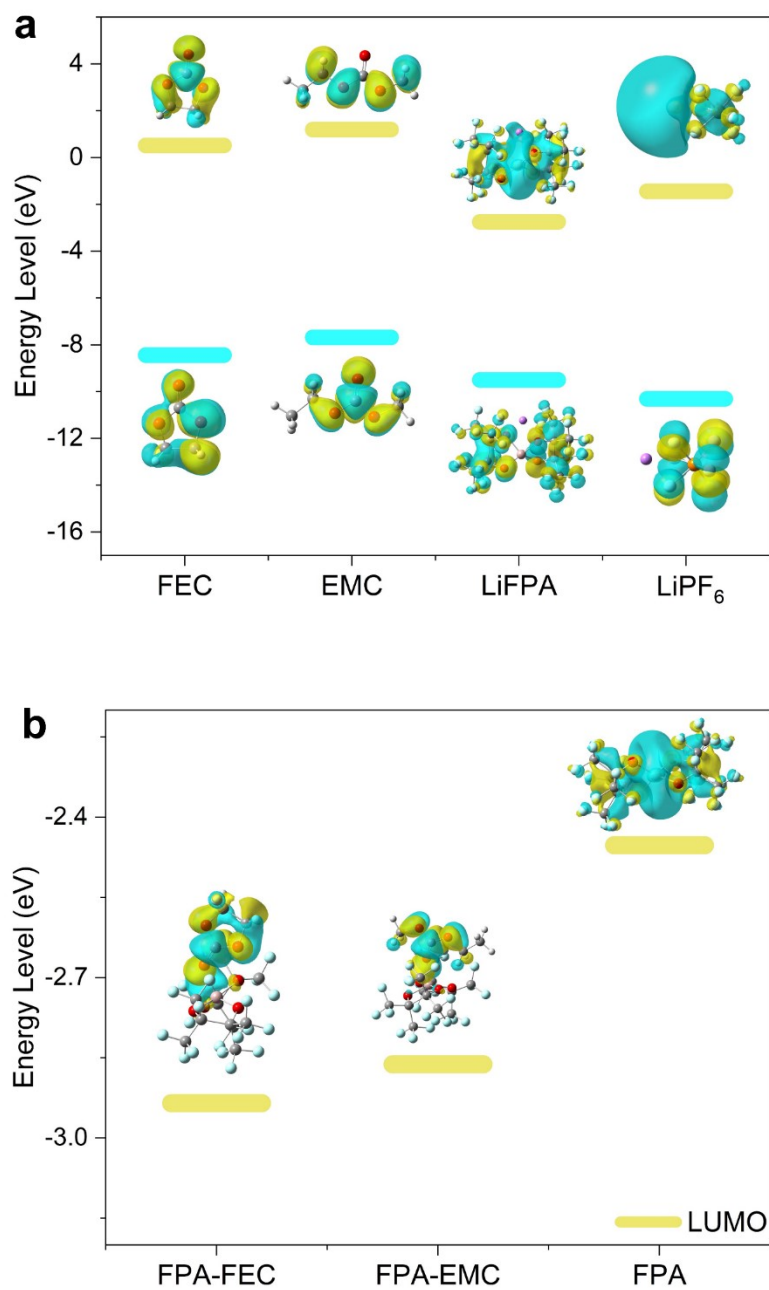


Fig. S10 | (a) Calculated HOMO and LUMO energy levels of FEC, EMC, LiFPA and LiPF₆. (b) The LUMO energy levels of FPA⁻ anion, FPA-FEC, and FPA-EMC.

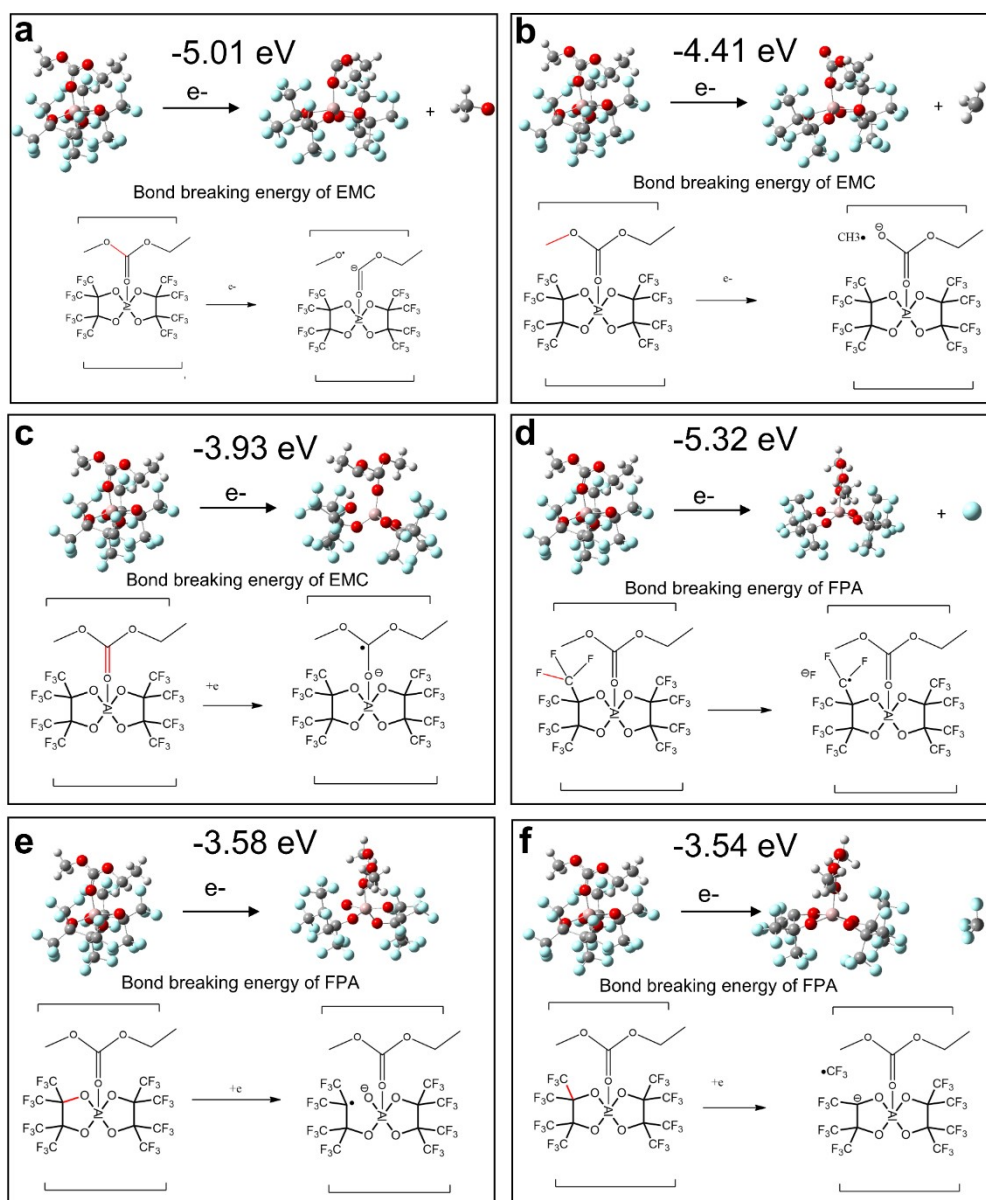


Fig. S11 | The calculated reductive bond-breaking energy of FPA-EMC in different bond-breaking ways. Fig. S11a-c is the bond breaking of EMC, Fig. S11d-f is the bond breaking of FPA⁻.

Fig. S11 show that several representative bond-breaking modes of FPA-EMC (**Fig. S11a-c** is the bond breaking of EMC and **Fig. S11d-f** is the bond breaking of FPA⁻) had been predicted by using DFT simulations. One can note that the C-F bond from FPA⁻ was preferentially broken due to the lowest bond breaking energy (**Fig. S11d**, -5.32 eV), when the FPA-EMC gets electrons.

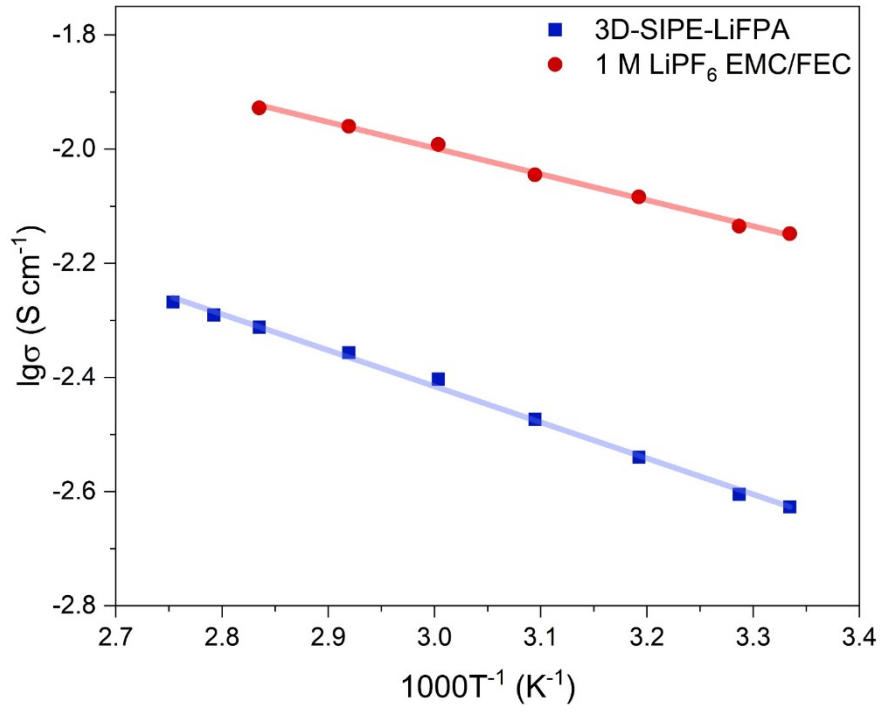


Fig. S12 | Ionic conductivities of as-constructed 3D-SIPE-LiFPA and 1 M LiPF₆ EMC/FEC at varied temperatures.

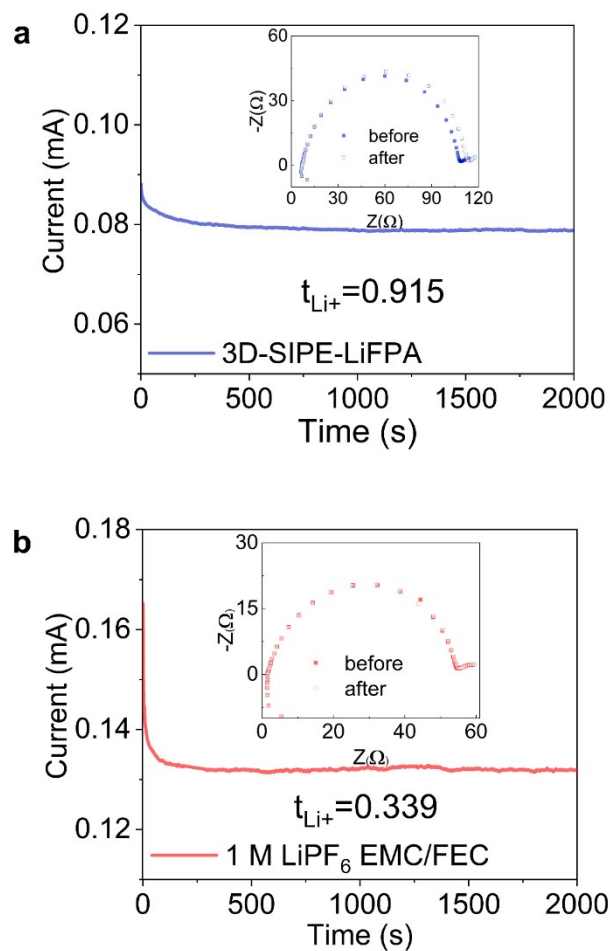


Fig. S13 | The t_{Li^+} of (a) 3D-SIPE-LiFPA and (b) 1 M LiPF₆ EMC/FEC.

The as-constructed 3D-SIPE-LiFPA (0.915) possesses larger t_{Li^+} than 1 M LiPF₆ EMC/FEC (0.339).

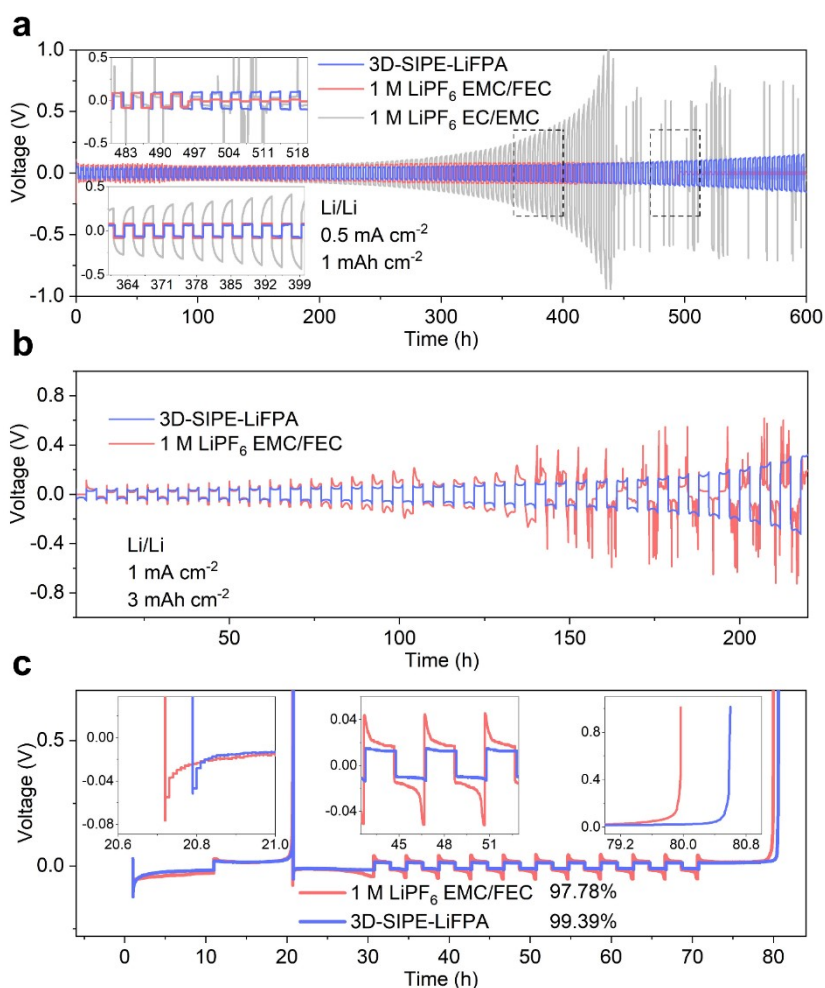


Fig. S14 | (a) Voltage profiles of Li/Li symmetrical cells in 3D-SIPE-LiFPA, 1 M LiPF₆ EMC/FEC and 1 M LiPF₆ EC/EMC, at a current density of 0.5 mA cm⁻² and a capacity of 1 mAh cm⁻². (b) Voltage profiles of Li/Li symmetrical cells, under a current density of 1 mA cm⁻² and capacity of 3 mAh cm⁻². (c) The CE of the Li/Cu asymmetrical cells measures by modified Aurbach's measurement using different electrolytes.

The interfacial stability between Li metal and electrolyte is evaluated using Li/Li cells and Li/Cu cells. As shown in **Fig. S14a** and **Fig. S14b**, Li/Li cells using as-constructed 3D-SIPE-LiFPA present more stable voltage profiles at 0.5 mA cm⁻² (1 mAh cm⁻²) and 1 mA cm⁻² (3 mAh cm⁻²). Moreover, 3D-SIPE-LiFPA enables Li/Cu cells with Coulombic efficiency (CE) of 99.39% measuring by modified Aurbach's measurement, which is much higher than the LiPF₆ based counterpart (**Fig. S14c**). Additionally, lower nucleation potential and lower overpotential are observed in the 3D-SIPE-LiFPA based Li/Cu cell. The low overpotential and impressive CE of the 3D-SIPE-LiFPA based cell confirm its high Li metal compatibility and respectable conductivity.

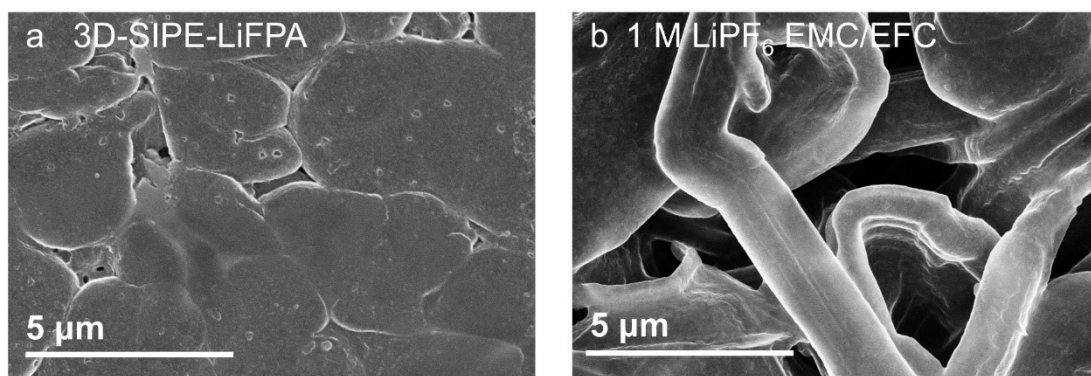


Fig. S15 | SEM images of deposited Li. Surface morphology of the deposited Li on Cu foil substrate using (a) as-papered 3D-SIPE-LiFPA and (b) 1 M LiPF₆ EC/EMC, at a current density of 0.5 mA cm⁻² with a capacity of 3 mAh cm⁻².

The deposited Li in 3D-SIPE-LiFPA displays a chunk morphology without dendrite (**Fig. S15a**), while a needle-like dendrite was observed in 1 M LiPF₆ EC/EMC (**Fig. S15b**). The large Li chunks without tortuosity in 3D-SIPE-LiFPA can maintain continuous contact with bulk Li during stripping process, reducing the amount of “dead” Li and obtaining high CE (**Fig. S14c**). In contrast, dendrite Li with large tortuosity in 1 M LiPF₆ EC/EMC will result in large amount of “dead” Li, causing low CE.

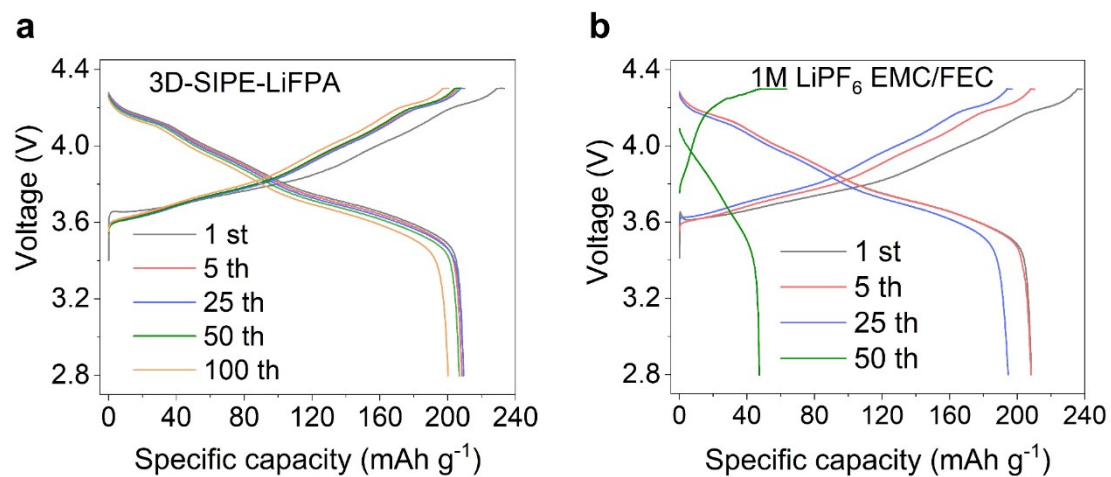


Fig. S16 | Charge/discharge curves of NCM811/Li LMBs (2.8-4.3 V, 3.7 mAh cm⁻², 50 μm Li) using (a) 3D-SIPE-LiFPA and (b) 1 M LiPF₆ EMC/FEC.

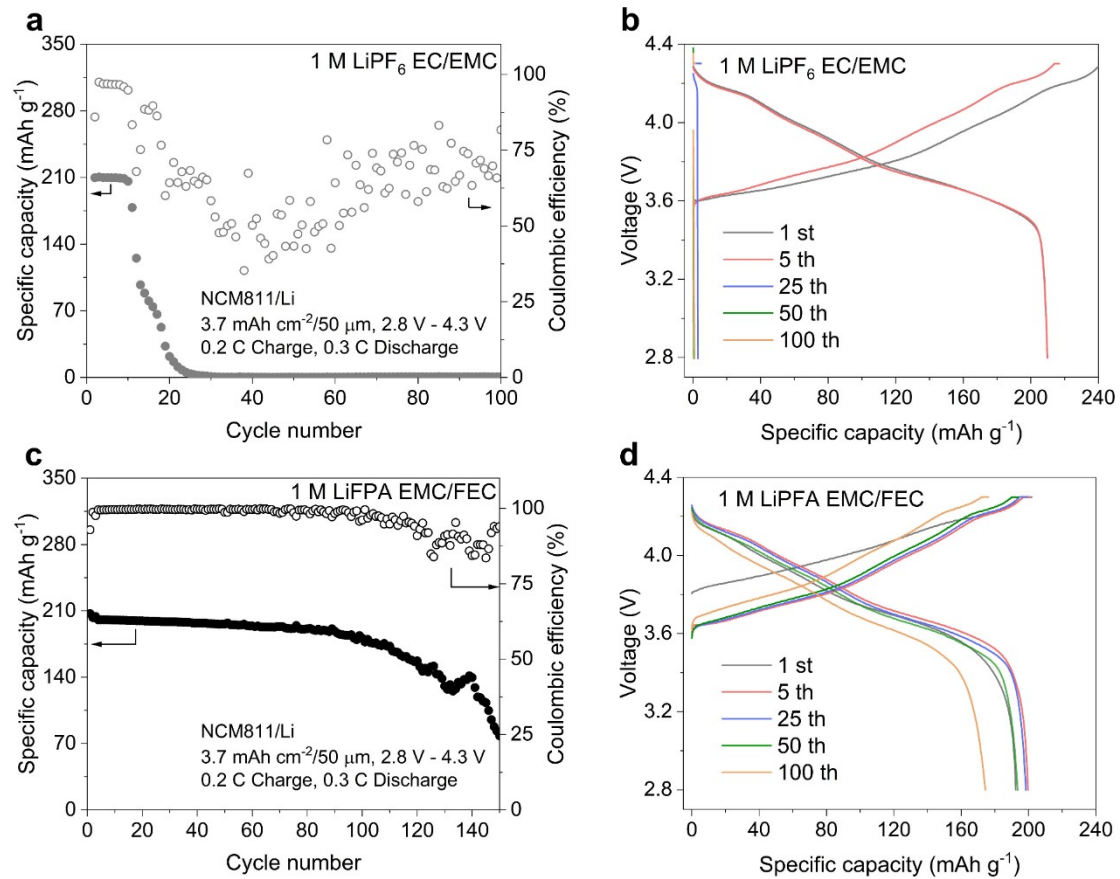


Fig. S17 | (a) Cycling performance of NCM811/Li LMBs (2.8-4.3 V, 3.7 mAh cm⁻², 50 μm Li) using 1 M LiPF₆ EC/EMC. (b) And representative charge/discharge curves. (c) Cycling performance of NCM811/Li LMBs (2.8-4.3 V, 3.7 mAh cm⁻², 50 μm Li) using 1 M LiFPA EMC/FEC. (d) And representative charge/discharge curves.

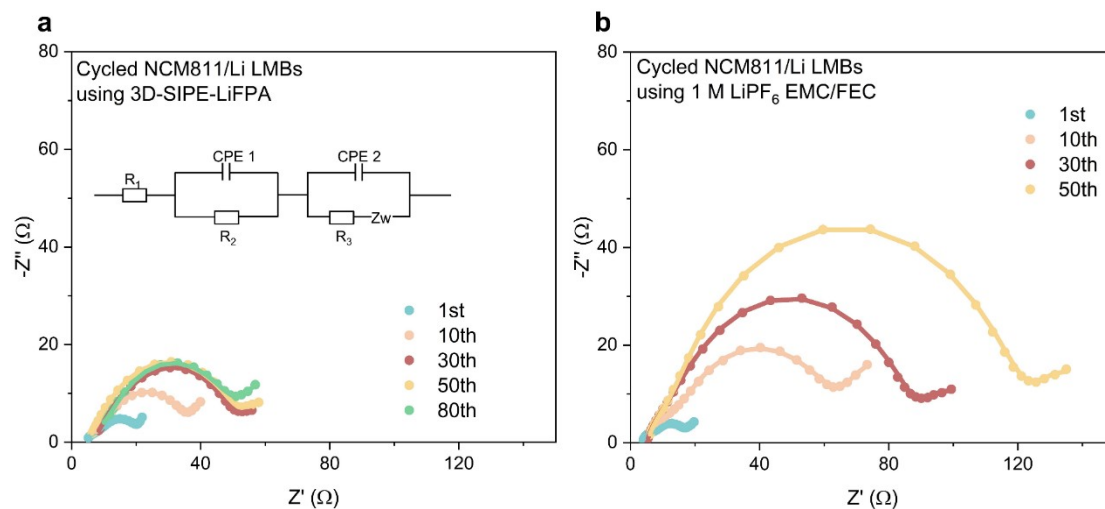


Fig. S18 | Nyquist plots of NCM811/Li LMBs at different cycles using (a) 3D-SIPE-LiFPA and (b) 1 M LiPF₆ EMC/FEC.

The EIS data (Nyquist plots) of cycled NCM811/Li LMBs using 3D-SIPE-LiFPA and 1 M LiPF₆ EMC/FEC are shown in **Fig. S18**. Then, the interfacial resistance of NCM811/Li LMBs using 3D-SIPE-LiFPA is low (12.0 Ω) at the 1st cycle and increase to *ca.* 45.3 Ω at the 30th cycle and keeps stable from the 30th to the 80th cycle. While the counterpart continuously increases from 12.3 Ω at the 1st cycle to 120.1 Ω at the 50th cycle and the battery gets capacity failure. Thus, the 3D-SIPE-LiFPA can form a more stable interface in NCM811/Li LMBs.

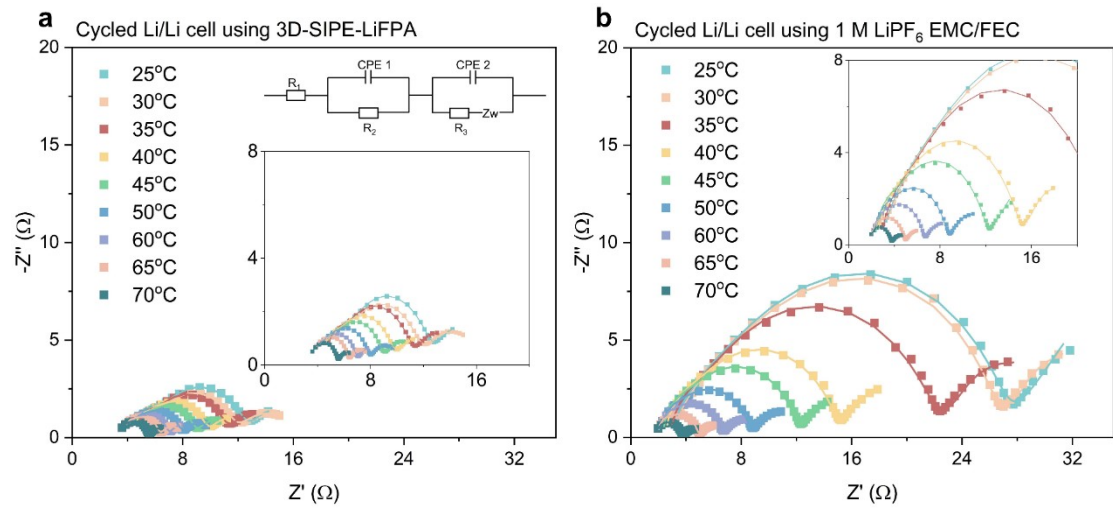


Fig. S19 | Nyquist plots of the Li/Li symmetrical cells (cycled at 25 °C for 10 cycles) at different temperatures.

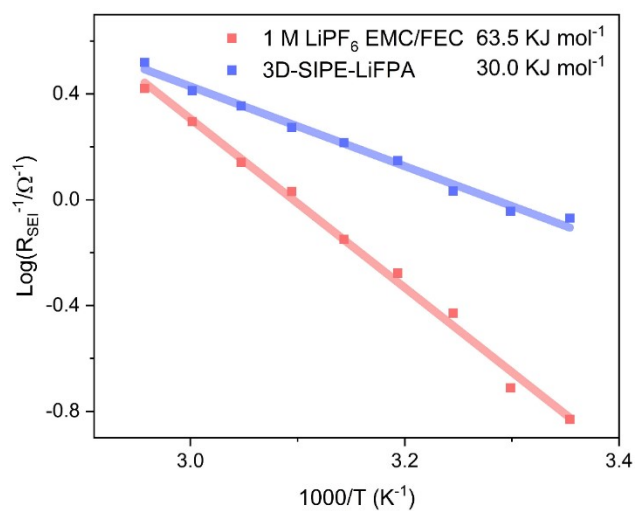


Fig. S20 | Arrhenius behavior and the activation energy of Li⁺ diffusion through SEI layers in Li/Li symmetrical cells.

The interfacial impedance of Li/Li symmetrical cells is shown in **Fig. S19**. One can note that the Li/Li symmetrical cell using 3D-SIPE-LiFPA has lower interfacial impedance (6.4 Ω) than that of contrast sample (24.2 Ω) at 25°C. The activation energy of Li⁺ diffusion through SEI layers was also calculated (**Fig. S20**). The 3D-SIPE-LiFPA based Li/Li symmetrical cell displays a lower activation energy (30.0 kJ mol⁻¹) compared with its contrast sample (63.5 kJ mol⁻¹), illustrating that 3D-SIPE-LiFPA induces the formation of a highly conductive SEI layer on the Li anode.

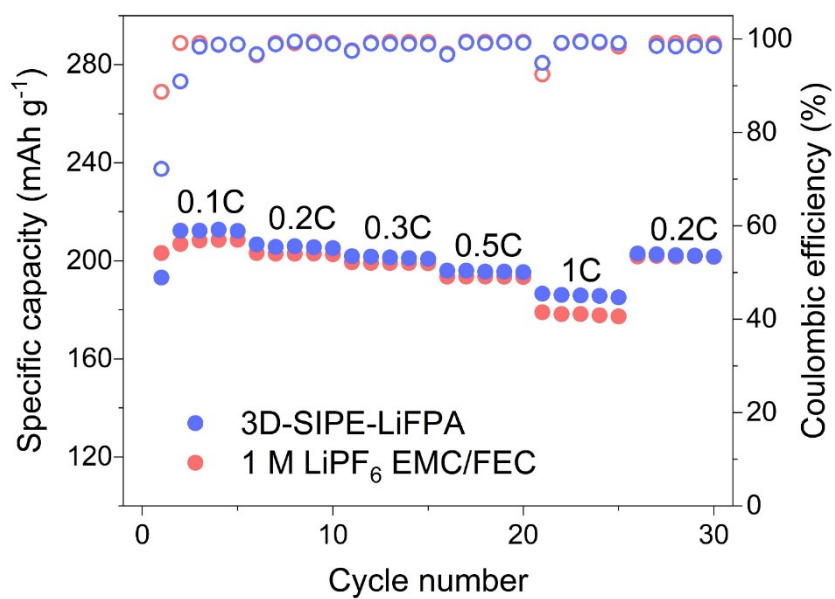


Fig. S21 | (a) Rate performance of NCM811/Li LMBs (2.8-4.3 V, 3.7 mAh cm⁻², 50 μm Li) using 3D-SIPE-LiFPA and 1 M LiPF₆ EMC/FEC.

As for rate capability, NCM811/Li LMBs (2.8-4.3 V) using 3D-SIPE-LiFPA offer a slightly higher capacity retention (87.9 %, 186.6 mA h g⁻¹ at 1 C rate, 212.3 mA h g⁻¹ at 0.1 C rate) than the counterpart (85.0 %, 177.3 mA h g⁻¹ at 1 C rate, and 208.6 mA h g⁻¹ at 0.1 C rate).

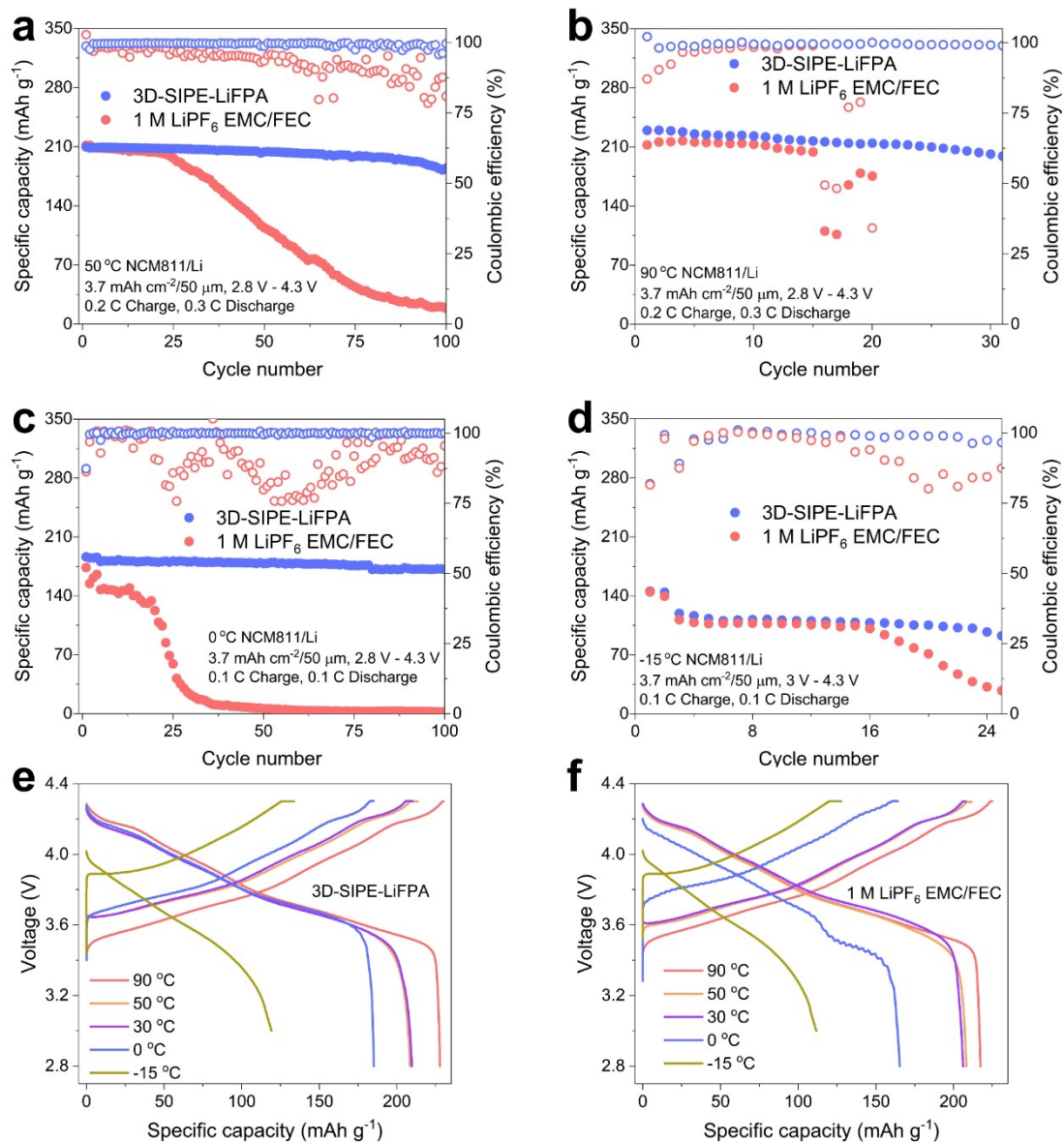


Fig. S22 | Cycling performance of NCM811/Li LMBs (2.8-4.3 V, 3.7 mAh cm⁻², 50 μm Li) at (a) 50 °C, (b) 90 °C, (c) 0 °C, (d) -15 °C. And representative charge-discharge curves of NCM811/Li LMBs using (e) 3D-SIPE-LiFPA and (f) 1 M LiPF₆ EMC/FEC.

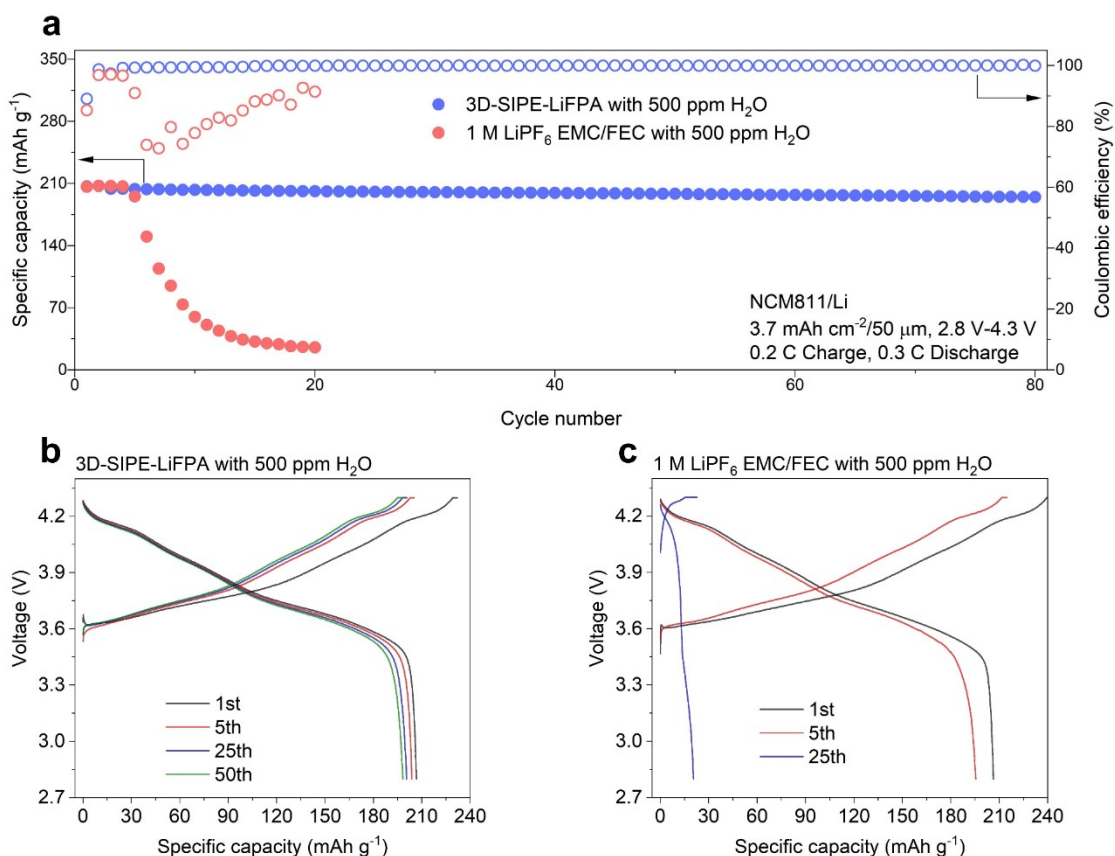


Fig. S23 | (a) Cycling performance of NCM811/Li LMBs (2.8-4.3 V, 3.7 mAh cm^{-2} , $50 \mu\text{m}$ Li) using different electrolytes. The representative charge/discharge curves of NCM811/Li LMBs using (b) 3D-SIPE-LiFPA with 500 ppm H_2O and (c) 1 M LiPF_6 EMC/FEC with 500 ppm H_2O , respectively.

We determined the water content of as-prepared 3D-SIPE-LiFPA and 1 M LiPF_6 EMC/FEC by Karl Fischer titration (WKT-A9). All the experimental processes were conducted in an Ar glovebox to prevent moisture contamination. The water content in all as-prepared electrolytes is less than 30 ppm. Then, we formulated two kinds of electrolytes with higher water content (3D-SIPE-LiFPA with 500 ppm H_2O and 1 M LiPF_6 EMC/FEC with 500 ppm H_2O) and tested the cycle performance of NCM811/Li LMBs (2.8-4.3 V, 3.7 mAh cm^{-2} , $50 \mu\text{m}$ Li) using as-prepared electrolytes (**Fig. S23**). The NCM811/Li LMB using 1 M LiPF_6 EMC/FEC with 500 ppm H_2O suffers from sudden capacity failure within 10 cycles. In contrast, when using 3D-SIPE-LiFPA with 500 ppm H_2O , the NCM811/Li LMB deliver a high-capacity retention of 95.4% ($194.7 \text{ mAh g}^{-1}/204.1 \text{ mAh g}^{-1}$) after cycling for 80 cycles. Thus, different from the LiPF_6 -based electrolyte, a trace amount of water will not significantly impact LMBs using 3D-SIPE-LiFPA.

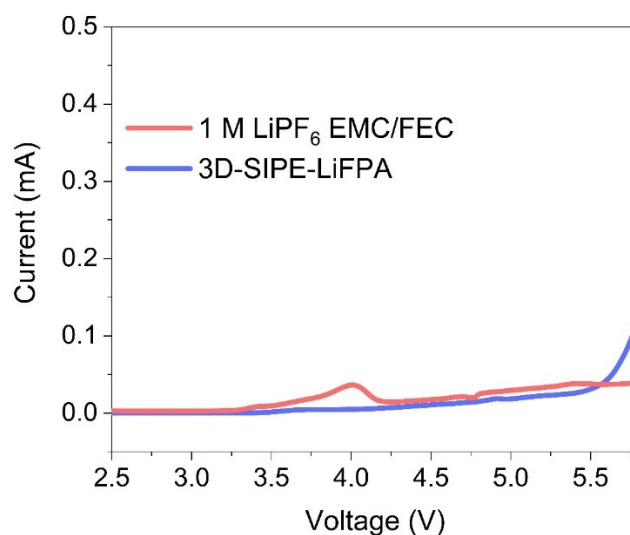


Fig. S24 | LSV curves of Li/SS asymmetrical cells at a scan rate of 1 mV s^{-1} .

The LSV curves of Li/SS half-cells using 1 M LiPF_6 EMC/FEC and 3D-SIPE-LiFPA are conducted and shown in **Fig. S24**. Obviously, the as-constructed 3D-SIPE-LiFPA is highly stable before 5.5 V (vs. Li/Li^+), while the counterpart of 1 M LiPF_6 EMC/FEC exhibits a significant oxidative peak at *ca.* 4.0 V and the oxidative current is higher than the 3D-SIPE-LiFPA before 5.5 V (vs. Li/Li^+). Therefore, in the working voltage range of LMBs, the as-constructed 3D-SIPE-LiFPA possesses superior oxidative stability.

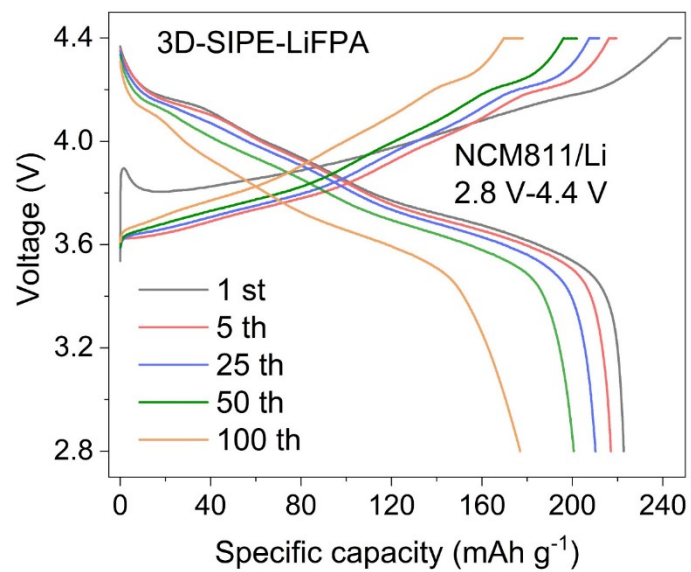


Fig. S25 | Representative charge-discharge curves of NCM811/Li LMBs at 2.8-4.4 V.

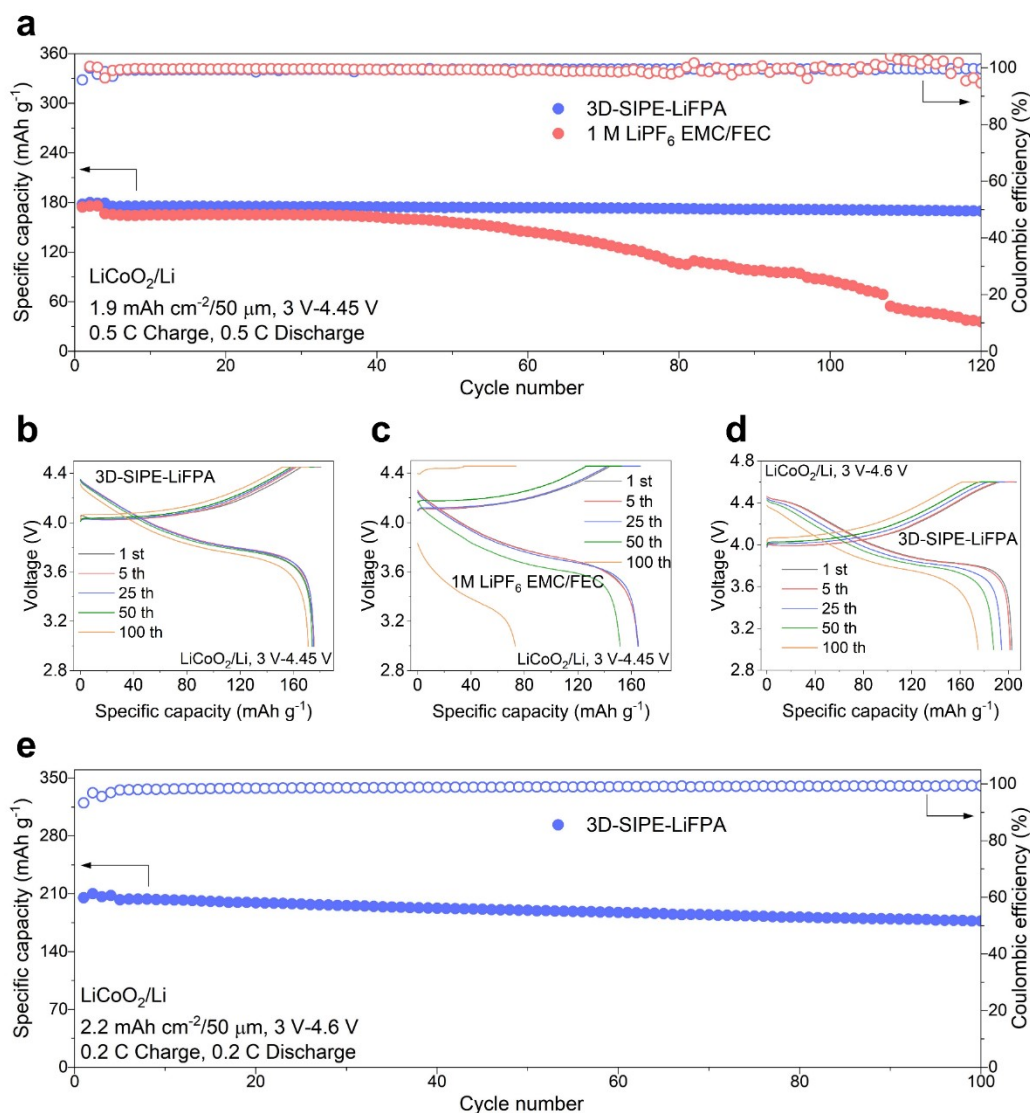


Fig. S26 | Cycling performance of LiCoO_2/Li LMBs. (a) Cycling performance of LiCoO_2/Li LMBs (3.0-4.45 V, 0.5 C, 1.9 mAh cm^{-2} , 50 μm Li). Representative charge/discharge curves of LiCoO_2/Li LMBs using (b) 3D-SIPE-LiFPA and (c) 1 M LiPF_6 EMC/FEC. (d, e) Cycling performance of LiCoO_2/Li LMB (3.0-4.6 V, 0.2 C, 2.2 mAh cm^{-2} , 50 μm Li) using 3D-SIPE-LiFPA.

As-constructed 3D-SIPE-LiFPA is evaluated in LiCoO_2/Li (3 V-4.45 V, 1.9 mAh cm^{-2} , 180 mAh g^{-1} ; 3 V-4.6 V, 2.2 mAh cm^{-2} , 210 mAh g^{-1}) LMBs to identify its universality. When charged/discharged at 0.5 C rate for 120 cycles, LiCoO_2/Li LMBs (2.8-4.45 V) using 3D-SIPE-LiFPA deliver a high-capacity retention of 96.9% (169.8 $\text{mAh g}^{-1}/175.2 \text{mAh g}^{-1}$) and a high average CE of 99.9% (**Fig. S26 a-b**). In contrast, LiCoO_2/Li LMBs using 1 M LiPF_6 EMC/FEC (**Fig. S26 a, c**) suffer from sudden capacity failure within 60 cycles. When the charge cut-off voltage is increased to 4.6 V, LiCoO_2/Li LMBs using 3D-SIPE-LiFPA still enable high cycling stability (87.2% capacity retention after 100 cycles, 177.1 $\text{mAh g}^{-1}/202.9 \text{mAh g}^{-1}$; average CE of 99.2%) (**Fig. S26 d-e**).

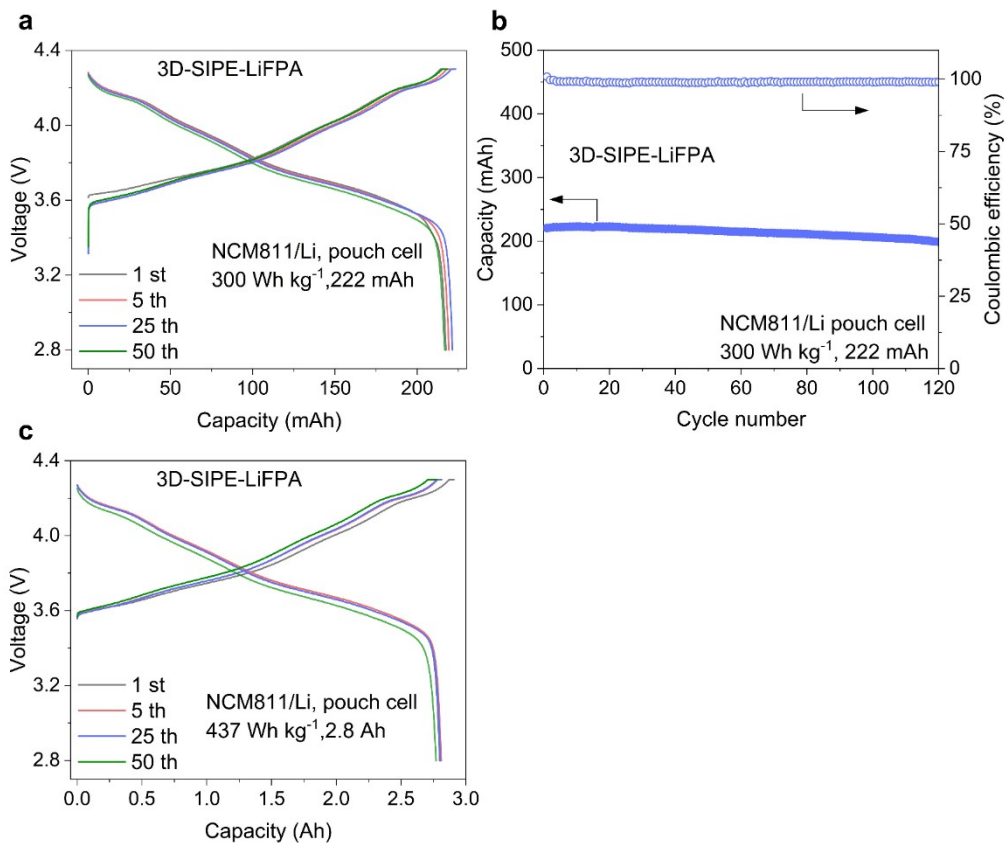


Fig. S27 | (a) Representative charge-discharge curves of pouch type NCM811/Li LMBs (300 Wh kg⁻¹, 222 mAh, 2.8-4.3 V, 3.7 mAh cm⁻², 50 μm Li) using 3D-SIPE-LiFPA. (b) And the corresponding cycling performance of 222 mAh NCM811/Li pouch cells using 3D-SIPE-LiFPA. (c) Representative charge-discharge curves of pouch type NCM811/Li LMBs (437 Wh kg⁻¹, 2.8 Ah, 2.8-4.3 V, 3.7 mAh cm⁻², 50 μm Li) using 3D-SIPE-LiFPA.

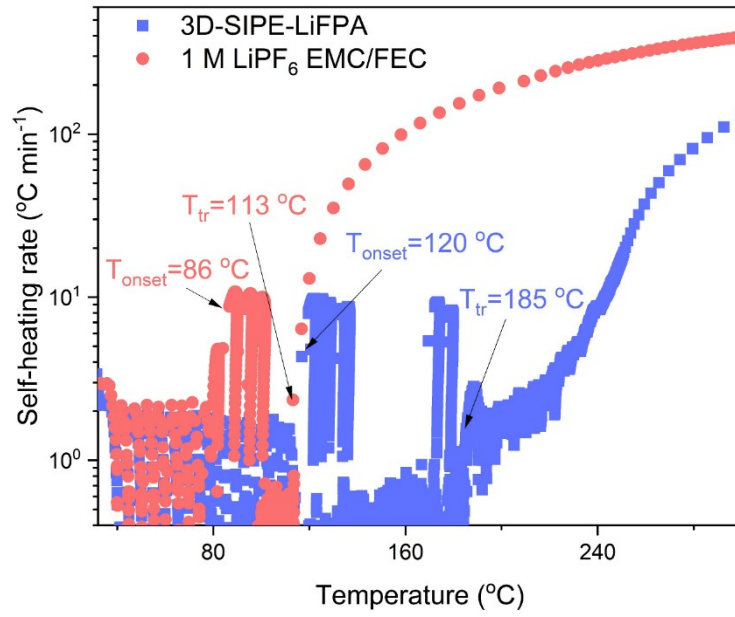


Fig. S28 | Self-heating rate (SHR) of 100% SOC NCM811/Li pouch cells using 3D-SIPE-LiFPA and 1 M LiPF₆ EMC/FEC under ARC tests.

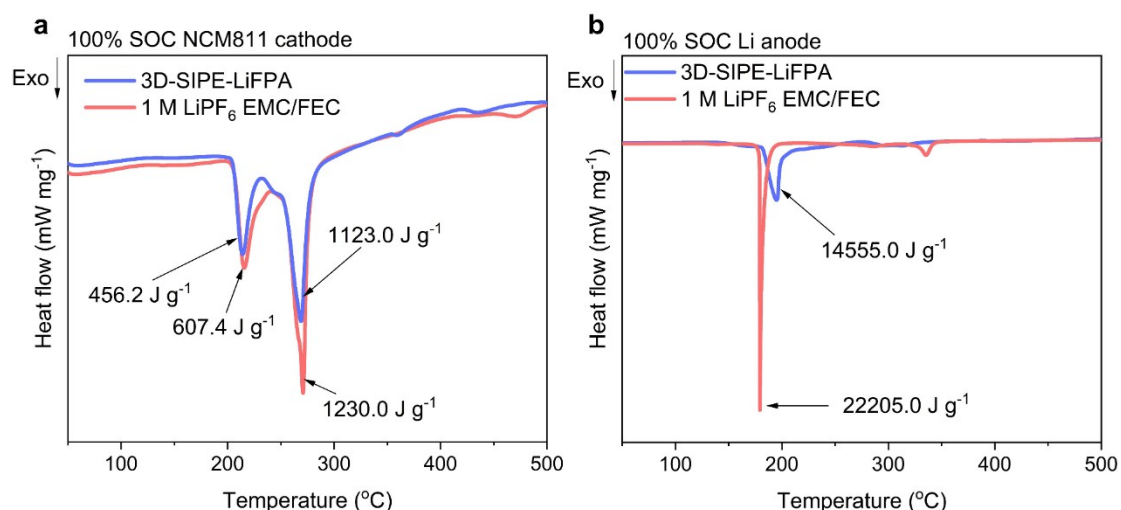


Fig. S29 | (a) DSC profiles of the 100% SOC NCM811 cathode. (b) DSC profiles of the 100% SOC Li anode.

The fully delithiated NCM811 cathode (abbreviated as 100% SOC NCM811 cathode) and Li anode with deposited Li (abbreviated as 100% SOC Li anode) were disassembled from 100% SOC NCM811/Li pouch cells. As shown in **Fig. S29**, the DSC measurement was employed to illustrate the thermal stability of 100% SOC NCM811 cathode (original wet state without adding additional electrolyte) and 100% SOC Li anode (original wet state without adding additional electrolyte). When using the counterpart electrolyte of 1 M LiPF₆ EMC/FEC, one can note that compared with 100% SOC NCM811 cathode, 100% SOC Li anode will release much more heat (22205.0 J g⁻¹ vs 1837.4 J g⁻¹) in temperature range of 50 °C-500 °C. This phenomenon clearly tells us that Li anode plays a dominate role in triggering the thermal runaway of NCM811/Li LMBs. In **Fig. S29a**, when using the as-constructed 3D-SIPE-LiFPA, 100% SOC NCM811 cathode shows two exothermic peaks at *ca.* 214 °C and *ca.* 270 °C with lower enthalpy change (456.2 J g⁻¹ and 1123.0 J g⁻¹, respectively; total = 1597.2 J g⁻¹) than the counterpart using 1 M LiPF₆ EMC/FEC (607.4 J g⁻¹ and 1230.0 J g⁻¹, respectively; total = 1837.4 J g⁻¹). The enthalpy change of 100% SOC Li anode is also reduced by *ca.* 35% when using 3D-SIPE-LiFPA (14555.0 J g⁻¹ vs. 22205.0 J g⁻¹, **Fig. S29b**). Meanwhile, the 100% SOC Li anode, using 1 M LiPF₆ EMC/FEC, suffers from sharp heat releasing centered at 178 °C (heat releasing temperature range 170 °C-192 °C). When using 3D-SIPE-LiFPA, the heat releasing peak of the 100% SOC Li anode is enhanced to 195 °C (heat releasing temperature range 181 °C-276 °C).

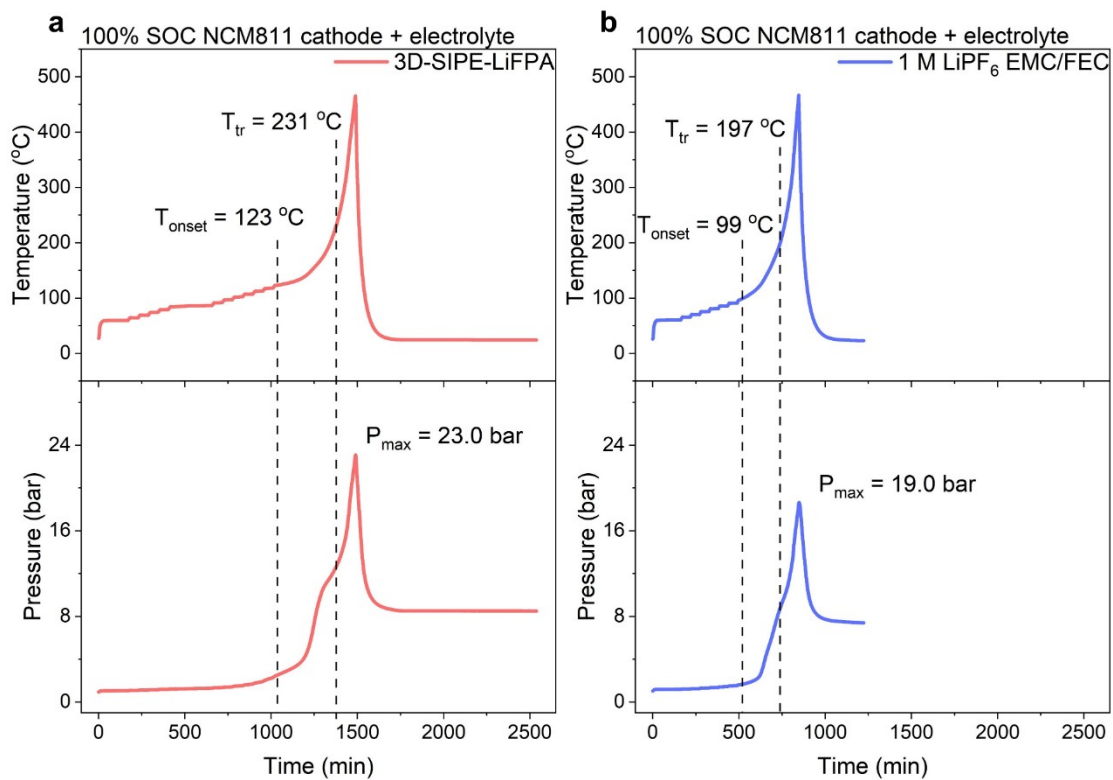


Fig. S30 | ARC measurement results of 100% SOC NCM811 cathode + electrolyte. (a) 3D-SIPE-LiFPA; (b) 1 M LiPF₆ EMC/FEC.

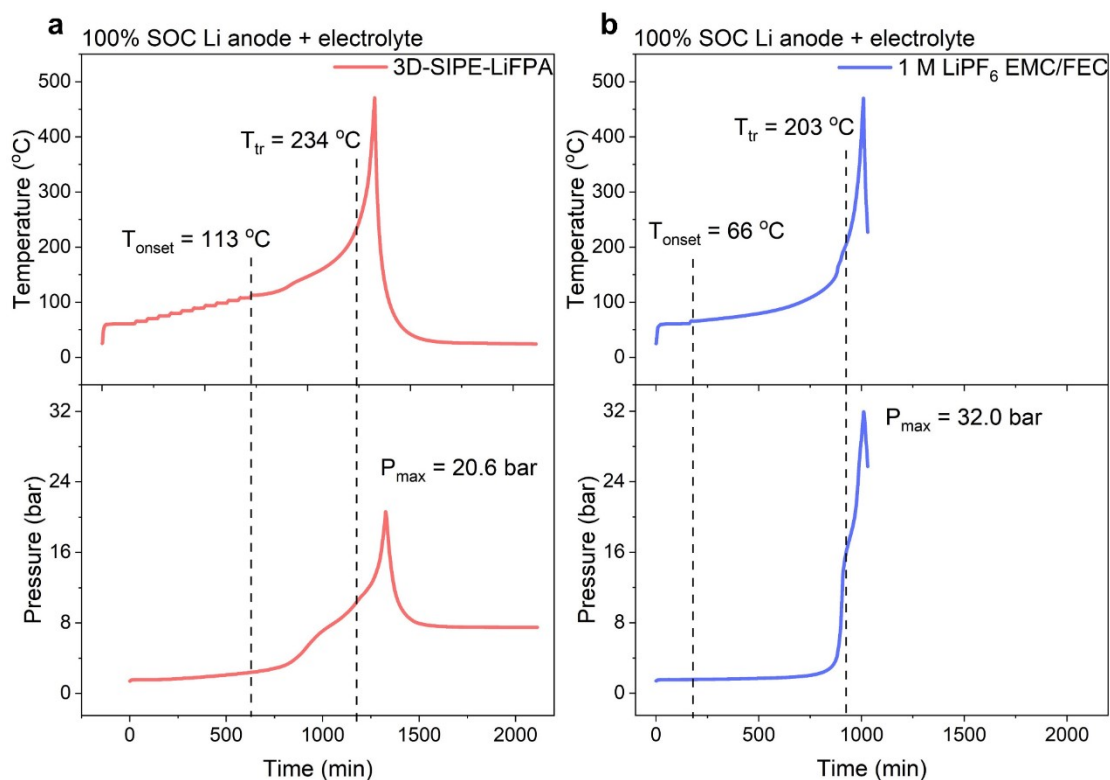


Fig. S31 | ARC measurement results of 100% SOC Li anode + electrolyte. (a) 3D-SIPE-LiFPA; (b) 1 M LiPF₆ EMC/FEC.

Next, the ARC test was also performed to elucidate the thermal stability of 100% SOC NCM811 cathode + electrolyte (abbreviated as cathode + electrolyte, 80 mg cathode materials + 500 μ L electrolyte, **Fig. S30**) and 100% SOC Li anode + electrolyte (abbreviated as anode + electrolyte, 80 mg anode materials + 500 μ L electrolyte, **Fig. S31**). Obviously, anode + electrolyte (**Fig. S31**) shows lower onset heat-releasing temperature (T_{onset}) in both electrolytes compared with cathode + electrolyte (**Fig. S30**). Both DSC and ARC measurements suggest that Li anode is determinant of the whole cell thermal runaway. In specific, when using 3D-SIPE-LiFPA, the T_{onset} and thermal runaway temperature (T_{tr}) of cathode + electrolyte increased to 123 °C (from 99 °C) and 231 °C (from 197 °C), respectively (**Fig. S30**). As for anode + electrolyte, T_{onset} and T_{tr} in ARC testing have also been enhanced by using 3D-SIPE-LiFPA (T_{onset} from 66°C to 113°C, T_{tr} from 203 °C to 234 °C, **Fig. S31**). Moreover, the pressure of generated gases from the exothermic reactions between Li anode and electrolyte are also significantly alleviated (**Fig. S31**, 32.0 bar vs. 20.6 bar). Therefore, the significantly enhanced safety characteristics of 100% SOC NCM811/Li pouch cells may originate

from the following main reasons: 1) The formation of a robust and thermally stable Li anode SEI layer enriched of LiF¹² and Al-containing species¹³; 2) The as-fabricated 3D-SIPE-LiFPA can help to alleviate the generation of thermal-induced gases from Li anode; 3) The poly-FPA anion chain can coordinate with EMC/FEC solvent molecules to immobilize the free solvents, alleviating the severe exothermic reactions between electrodes and electrolytes; 4) The highly fluorinated 3D cross-linked poly-FPA anion chain is thermally stable because of the large amounts of C-F bonds.¹⁴

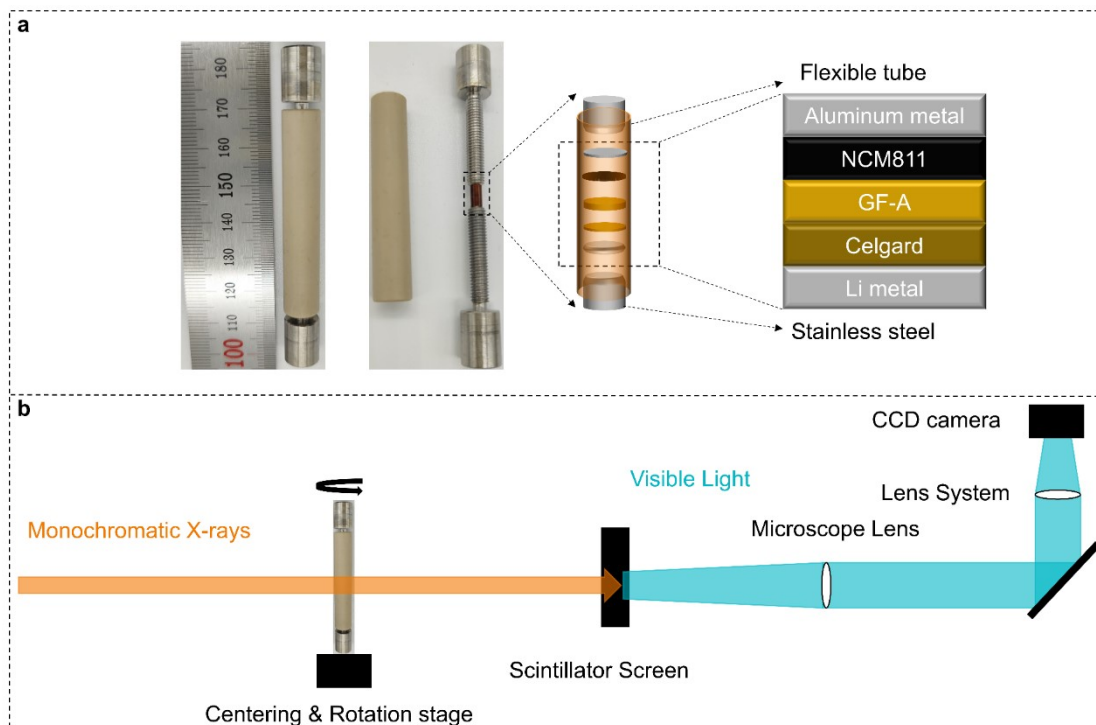


Fig. S32 | (a) The digital photograph and corresponding illustration of the employed customized tomography cells (tomo-cells). (b) The schematic illustration of the used beamline setup.

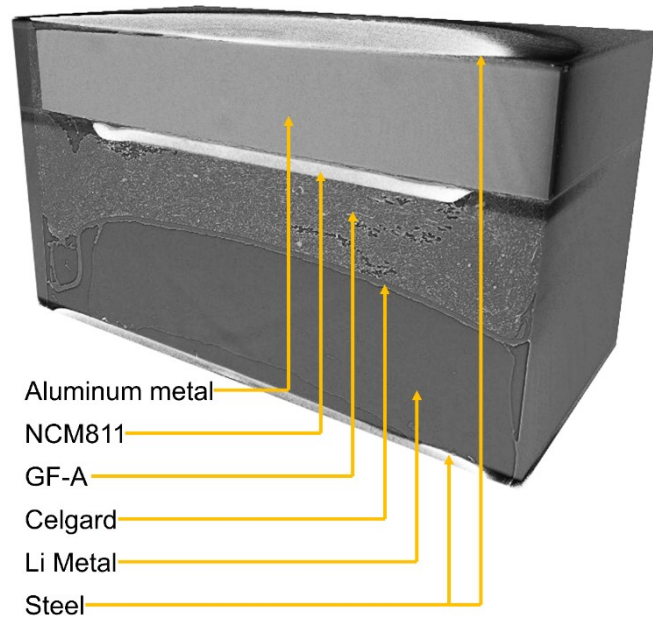


Fig. S33 | Selected tomography data of NCM811/Li cell (each component is clearly marked).

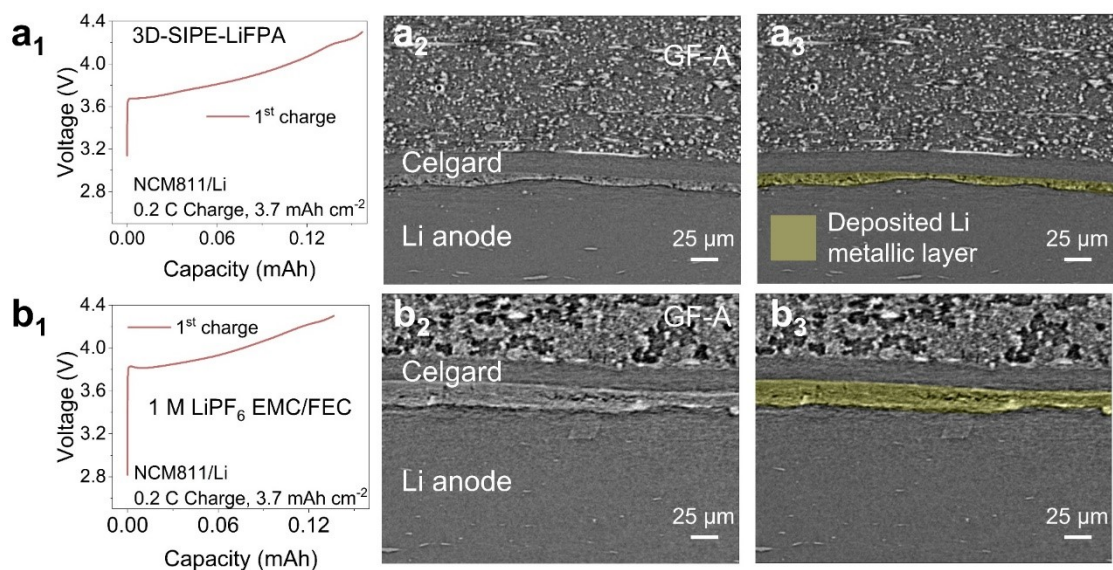


Fig. S34 | (a₁, b₁) Electrochemical performances of the studied NCM811/Li tomo-cells. (a₂, b₂) The corresponding X-ray tomography cross-sections of the studied NCM811/Li tomo-cells. (a₃, b₃) Rendered images of Fig. a₂, b₂. The studied tomo-cells were assembled with NCM811 cathode (3.7 mAh cm⁻², 2.8-4.3 V) and Li anode after first charging, using 3D-SIPE-LiFPA (a₁-a₃) and 1 M LiPF₆ EMC/FEC (b₁-b₃), respectively.

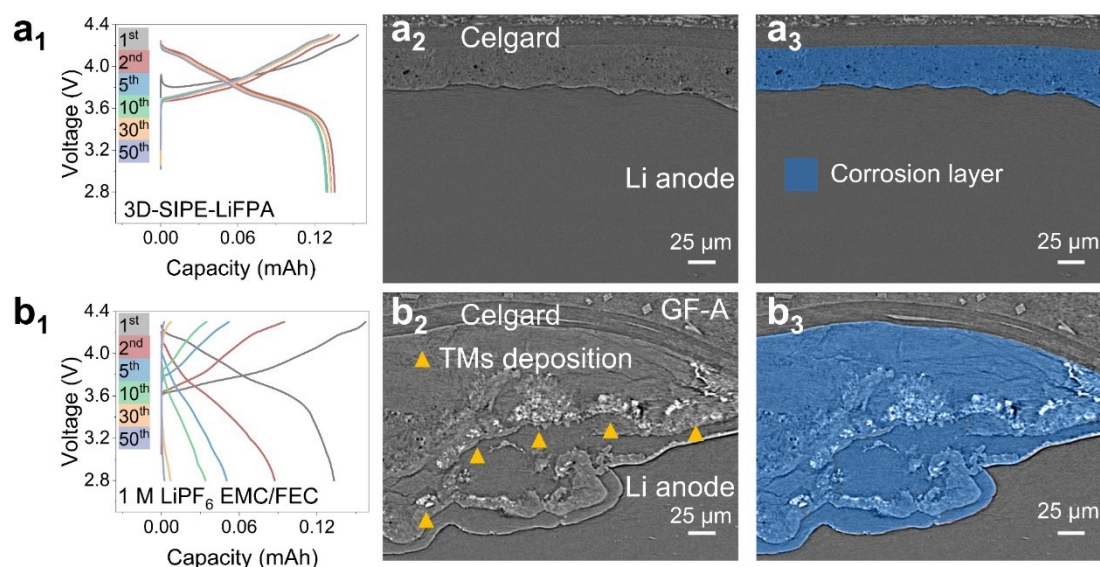
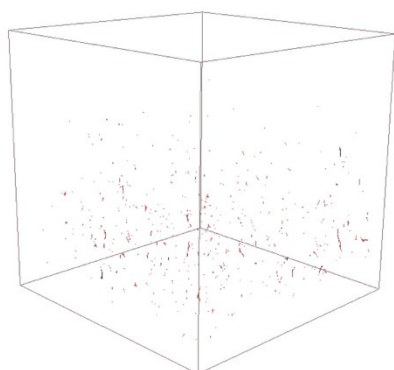


Fig. S35 | (a₁, b₁) Electrochemical performances of the studied NCM811/Li tomo-cells. (a₂, b₂) The corresponding X-ray tomography cross-sections of the studied NCM811/Li tomo-cells. (a₃, b₃) Rendered images of Fig. a₂, b₂. The studied tomo-cells were assembled with NCM811 cathode (3.7 mAh cm⁻², 2.8-4.3 V) and Li anode after 50 cycles, using 3D-SIPE-LiFPA (a₁-a₃) and 1 M LiPF₆ EMC/FEC (b₁-b₃), respectively.

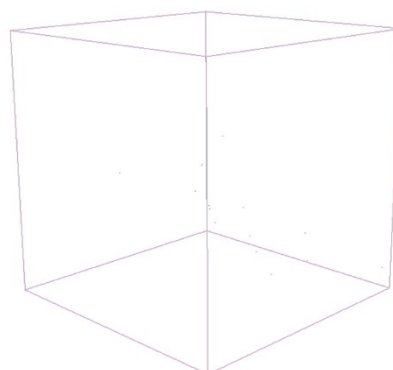
Fig. S35 show that more heterogeneous Li deposits and voids were generated in the NCM811/Li cells using 1 M LiPF₆ EMC/FEC electrolyte after 50 cycles. In addition, on can note that separator was mechanically deformed due to Li anode volume changes during Li stripping/plating. The generated Li deposits using 1 M LiPF₆ EMC/FEC electrolyte contain a large number of by-products, which reduce their electronic conductivity. So, during the subsequent stripping process, the remained Li bulk contacting the collector and having higher electronic conductivity will be preferentially stripped, resulting in the exposure of fresh Li surface and the solid electrolyte interphase (SEI) formation. During the plating process, the plated Li will be wrapped by the re-formed SEI again, forming inactive Li electrodeposits. As a result, the Li deposits layer thickens with increasing cycles.

a Li anode Ni deposition



1 M LiPF₆ EMC/FEC

b Li anode Ni deposition



3D-SIPE-LiFPA

Fig. S36 | ToF-SIMS 3D depth reconstruction of Li anode cycled in (a) 1 M LiPF₆ EMC/FEC and (b) 3D-SIPE-LiFPA. The Li anode was disassembled from NMC811/Li (3.7 mAh cm⁻², 50 μm Li) LMBs after 50 cycles.

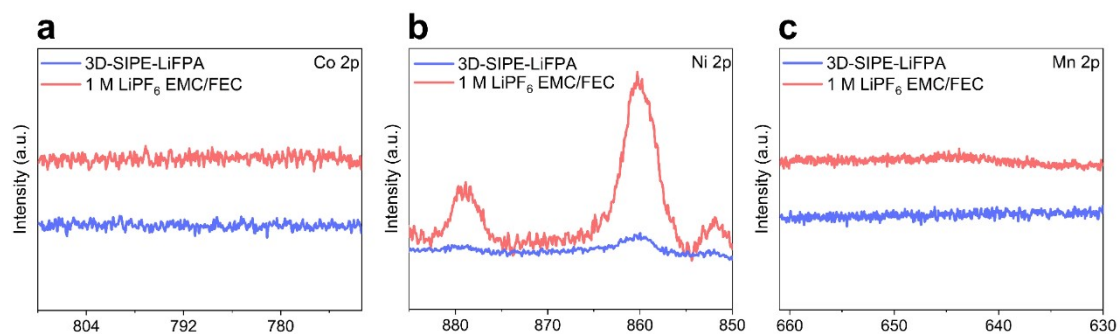


Fig. S37 | (a) Co 2p, (b) Ni 2p, (c) Mn 2p XPS spectra of Li anode cycled in 3D-SIPE-LiFPA and 1 M LiPF₆ EMC/FEC. The Li anode was disassembled from NMC811/Li (3.7 mAh cm⁻², 50 μm Li) LMBs after 50 cycles.

Fig. S36 and **Fig. S37** jointly show that 3D-SIPE-LiFPA could effectively inhibit cross-talk of Ni element from NCM811 cathode to Li anode.

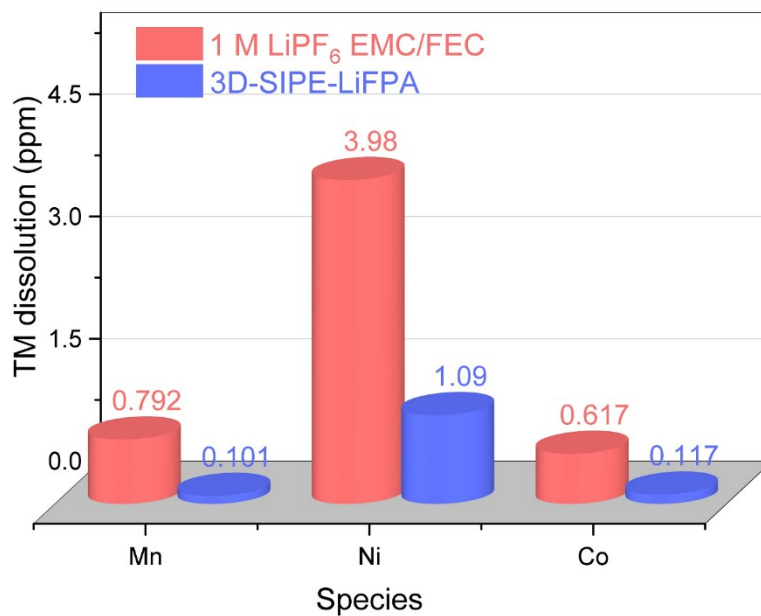


Fig. S38 | The amount of the dissolved TMs in separator (measured by ICP-MS). The GF-A separator was disassembled from NMC811/Li (3.7 mAh cm^{-2} , $50 \text{ }\mu\text{m Li}$) LMBs after 50 cycles.

The amount of dissolved Mn, Ni and Co, in separator when using 3D-SIPE-LiFPA, is 0.101 ppm, 1.09 ppm and 0.117 ppm, respectively. In sharp contrast, the amount of the dissolved Mn, Ni and Co, in separator when using 1 M LiPF₆ EMC/FEC, is 0.792 ppm, 3.98 ppm and 0.617 ppm, respectively. Thus, the as-constructed 3D-SIPE-LiFPA can inhibit TMs dissolution from the NCM811 cathode.

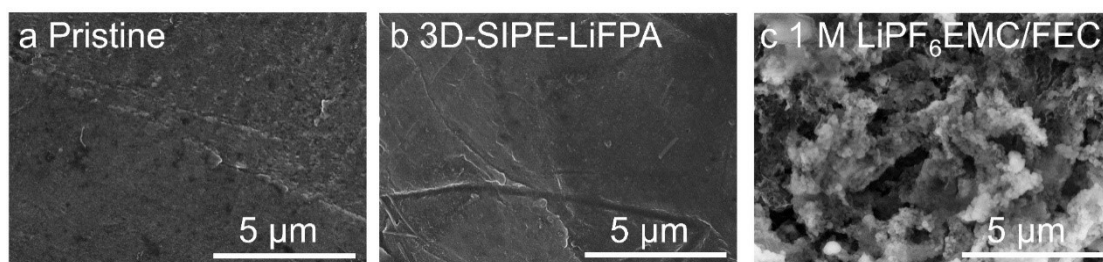


Fig. S39 | SEM images of top-view of the (a) pristine Li anode and Li anode cycled in (b) 3D-SIPE-LiFPA and (c) 1 M LiPF₆ EMC/FEC. The Li anode is disassembled from NMC811/Li (3.7 mAh cm⁻², 50 μm Li) LMBs after 50 cycles.

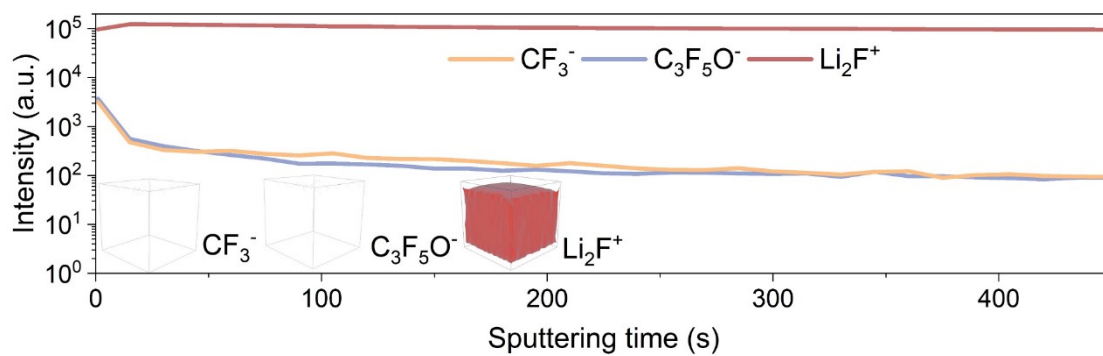


Fig. S40 | ToF-SIMS 3D reconstruction and corresponding depth profiles of Li anode cycled in 1 M $LiPF_6$ EMC/FEC. The Li anode is disassembled from NMC811/Li (3.7 mAh cm^{-2} , $50 \mu\text{m Li}$) LMBs after 50 cycles.

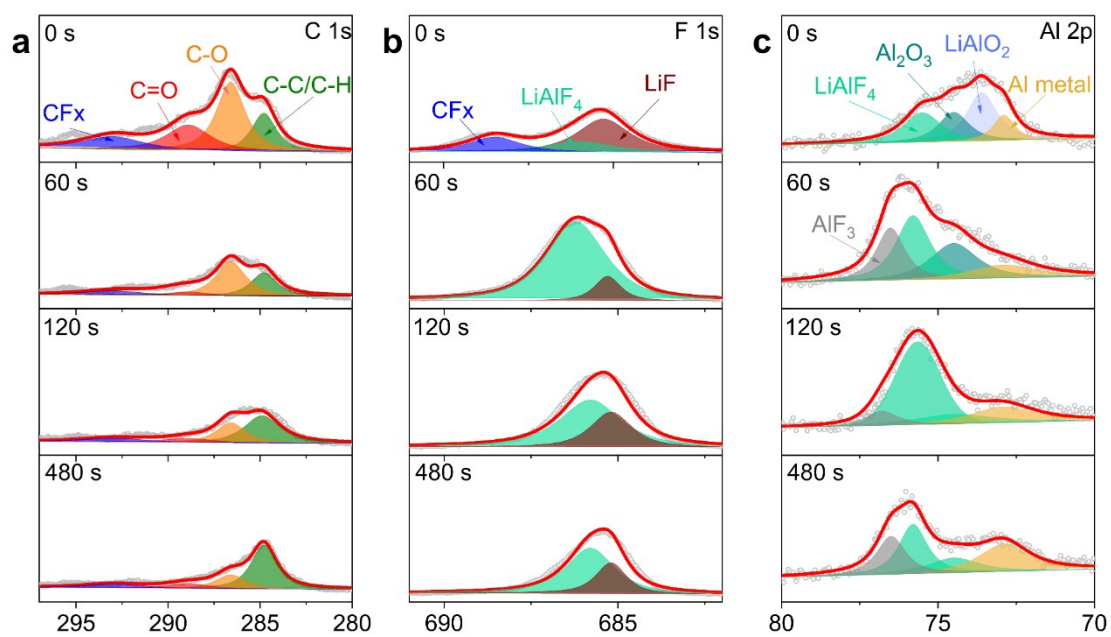


Fig. S41 | XPS spectra of Li anode after 50 cycles in NMC811/Li (3.7mAh cm^{-2} , $50\ \mu\text{m Li}$) LMBs using 3D-SIPE-LiFPA: (a) C 1s, (b) F 1s and (c) Al 2p.

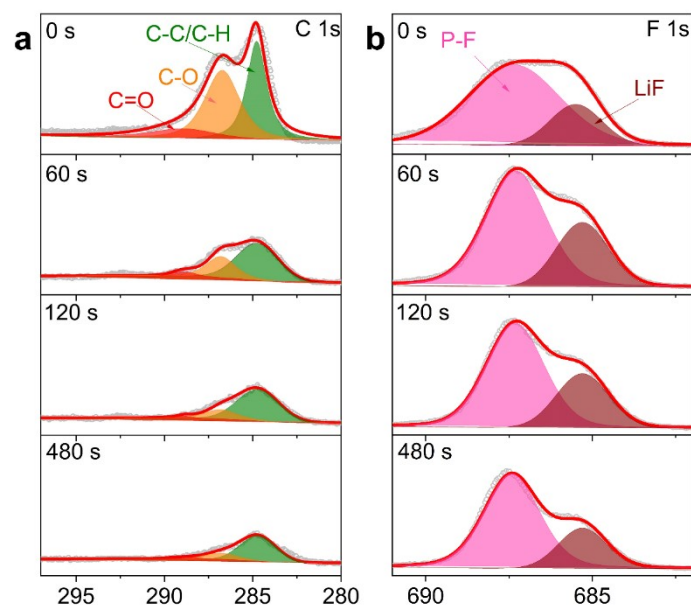


Fig. S42 | XPS spectra of Li anode after 50 cycles in NMC811/Li (3.7mAh cm^{-2} , $50\ \mu\text{m Li}$) LMBs using $1\ \text{M LiPF}_6$ EMC/FEC: (a) C 1s and (c) F 1s.

The ToF-SIMS result in Fig. S31 shows that almost no C-F species is detected on the Li anode cycled in $1\ \text{M LiPF}_6$ EMC/FEC. In XPS C1s spectra (**Fig. S41a** and **Fig. S42a**), the peaks at 284.8, 286.6, 288.9 and 293 eV are ascribed to C-C/C-H, C-O, C=O and CF_x , respectively. It is noted that the intensity of C-C/C-H peaks on Li cycled in 3D-SIPE-LiFPA is lower than that cycled in $1\ \text{M LiPF}_6$ EMC/FEC. Moreover, much P-F and LiF peaks are observed on the anode cycled in $1\ \text{M LiPF}_6$ EMC/FEC. These results indicate that the as-formed protective SEI in 3D-SIPE-LiFPA can efficiently suppress the decomposition of both solvent and lithium salts in electrolyte.

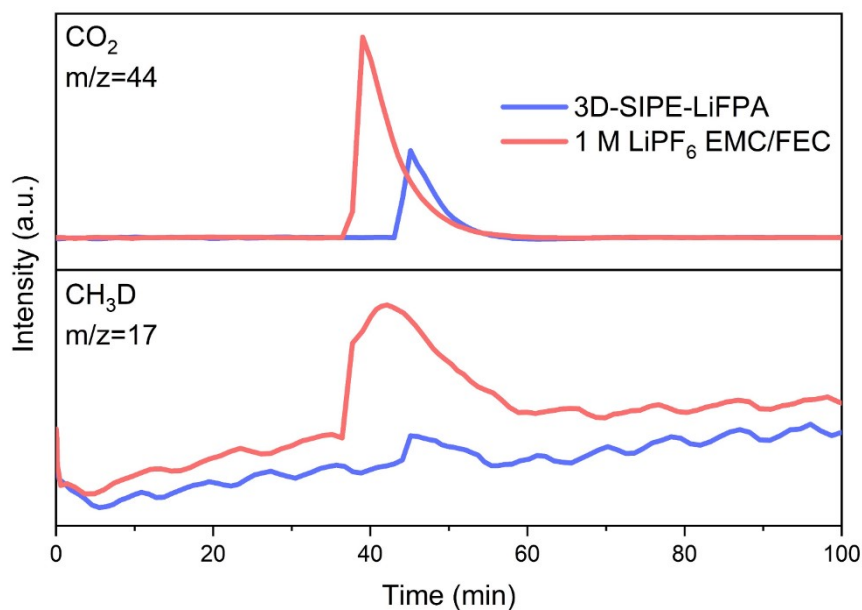
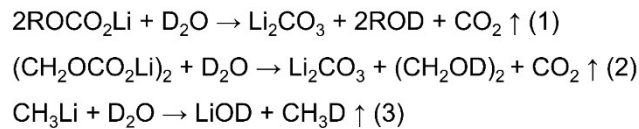


Fig. S43 | The CO_2 and CH_3D evolution rate curve after D_2O titration on Li anode cycled in 1 M LiPF_6 EMC/FEC and 3D-SIPE-LiFPA. The Li anode is disassembled from NMC811/Li (3.7 mAh cm^{-2} , $50 \mu\text{m}$ Li) LMBS after 50 cycles. The weight of samples is equal to 8 mg.

In previous reports, researchers believe that SEI layers of Li anodes are consisted with inorganic species (such as LiF , Li_2CO_3 , Li_2O , LiH , etc.) and organic species (such as ROCO_2Li , $(\text{CH}_2\text{OCO}_2\text{Li})_2$, CH_3Li , etc.). Therefore, some inorganic species and organic species can be quantified, utilizing the chemical reactivity between their and D_2O (such as the equation in **Fig. S43**).

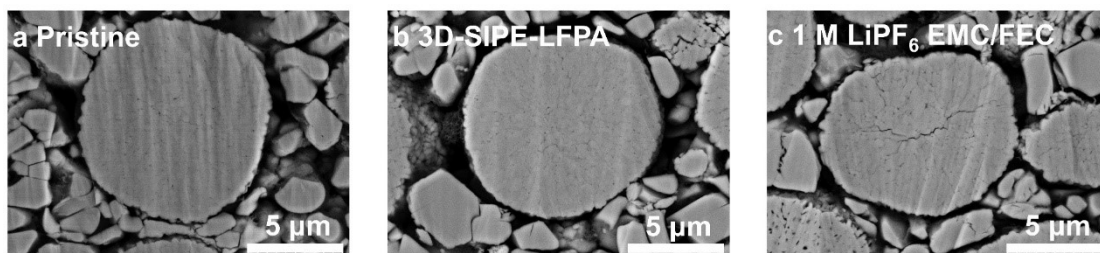


Fig. S44 | Cross-section SEM images of the (a) pristine NCM811 and NCM811 after 50 cycles using (b) 3D-SIPE-LiFPA, (c) 1 M LiPF₆ EMC/FEC.

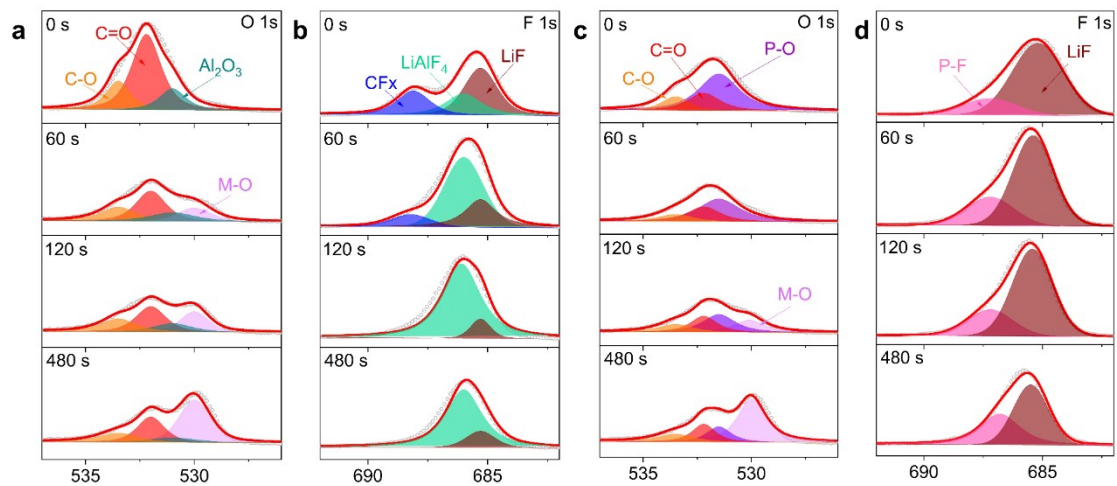


Fig. S45 | XPS spectra of selected elements of cathode/electrolyte interfaces (CEIs) on NCM811 particles after 50 cycles in NMC811/Li (3.7mAh cm^{-2} , $50\mu\text{m Li}$) LMBs using 3D-SIPE-LiFPA: (a, O 1s; b, F 1s) and 1 M LiPF₆ EMC/FEC (c, O 1s; d, F 1s).

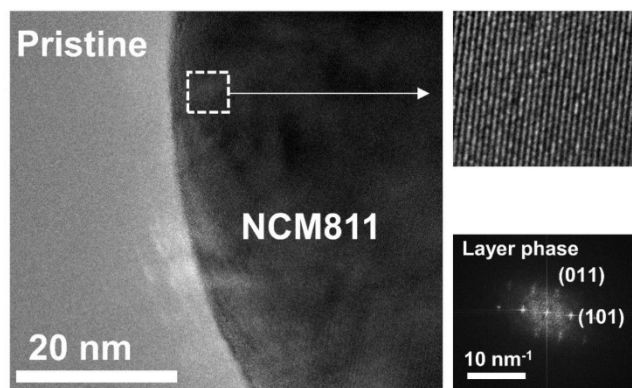


Fig. S46 | HRTEM analyses of the Pristine NCM811 cathode.

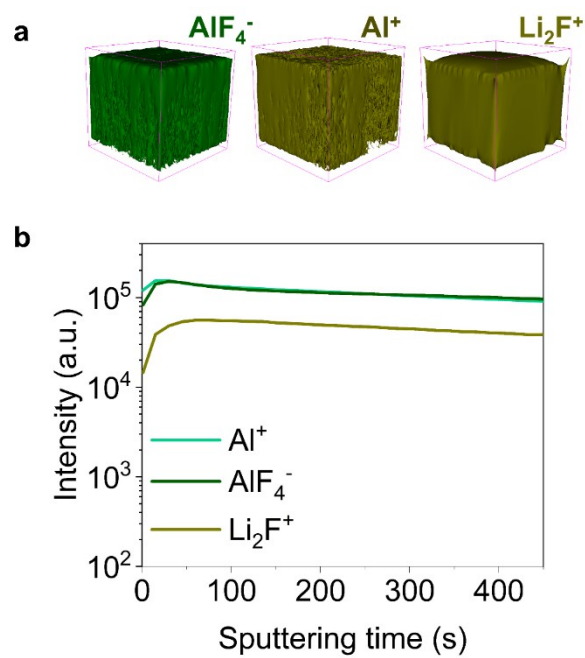


Fig. S47 | ToF-SIMS (a) 3D reconstruction and corresponding (b) depth profiles of NCM811 cathode. NCM811 cathode was disassembled from NMC811/Li (3.7 mAh cm^{-2} , $50 \text{ }\mu\text{m Li}$) LMBs after 50 cycles using the as-constructed 3D-SIPE-LiFPA.

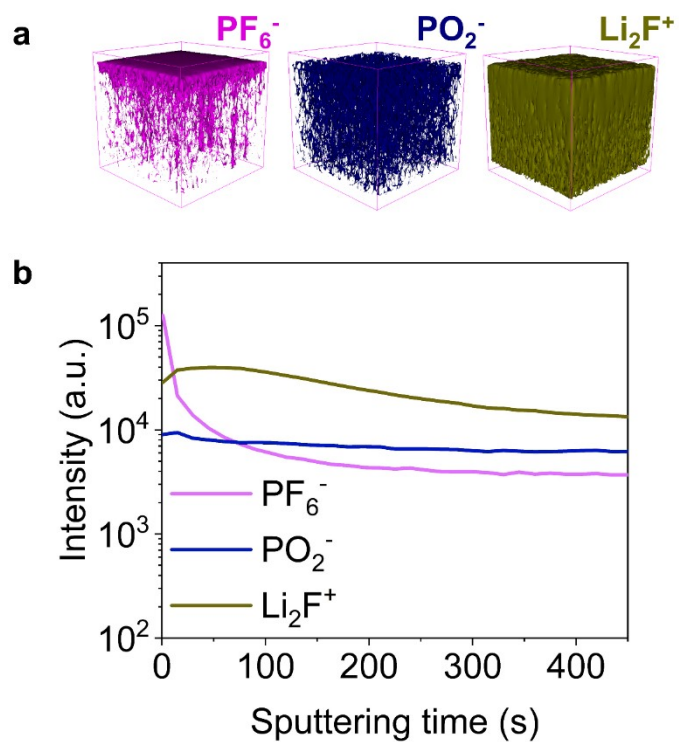


Fig. S48 | ToF-SIMS (a) 3D reconstruction and corresponding (b) depth profiles of NCM811 cathode. NCM811 cathode was disassembled from NMC811/Li (3.7 mAh cm^{-2} , $50 \text{ }\mu\text{m Li}$) LMBs after 50 cycles using 1 M LiPF_6 EMC/FEC.

Fig. S45c, d and **Fig. S48** show that more LiF, P-O and P-F species (indicating the decomposition of LiPF_6) are detected in the NCM811 cathode CEI, cycled in 1 M LiPF_6 EMC/FEC. With the decomposition of LiPF_6 , a large amount of HF will be produced.

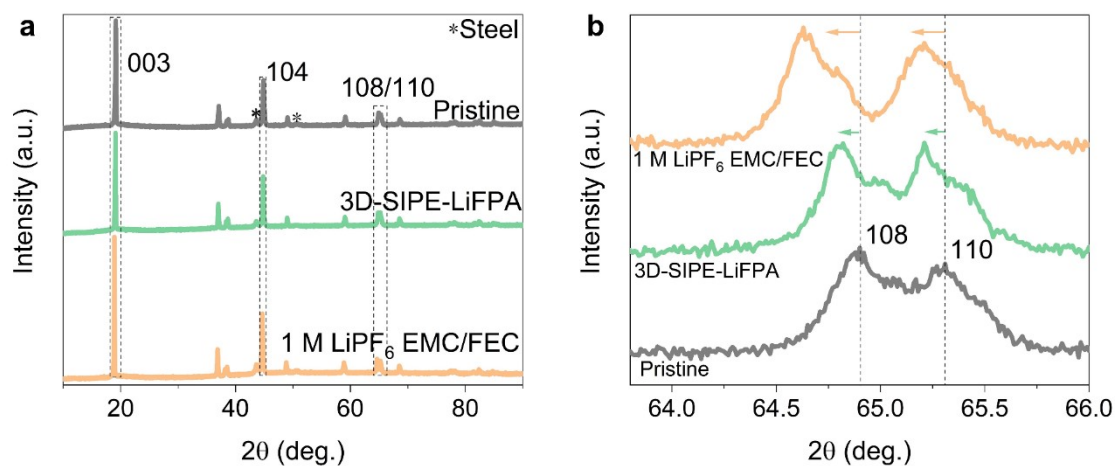


Fig. S49 | XRD of the NCM811 cathode. NCM811 cathode was disassembled from NMC811/Li (3.7 mAh cm⁻², 50 μ m Li) LMBs after 50 cycles using the as-constructed 3D-SIPE-LiFPA.

Fig. 6d and **Fig. S49** depicts XRD patterns of NCM811 cathodes of the (003) and (108)/(110) Bragg reflections, respectively. The former represents lattice changes along c-direction while latter represents that along a-direction. The shift and separation of the (003) and (108)/(110) peaks are lower in NCM811 cathode cycled using 3D-SIPE-LiFPA, suggesting its improved protection of NCM811 crystal structure.

Table S1 | Electrochemical performances of representative liquid state electrolytes for LMBs.

Approach	Formula	E/C ratio	Cell component	Cycling condition & capacity retention
This work	3D-SIPE-LiFPA	~10 g Ah⁻¹	NMC811/Li (3.7 mAh cm⁻²), N/P = 2.7	4.3 V, 0.2 C, 80.8 % after 236 cycles
This work pouch cell	3D-SIPE-LiFPA	~ 3.5 g Ah⁻¹	NMC811/Li (3.7 mAh cm⁻²), N/P = 2.7, 222 mAh, 300 Wh kg⁻¹	4.3 V, 0.2 C, 90.0 % after 120 cycles
This work pouch cell	3D-SIPE-LiFPA	~ 2 g Ah⁻¹	NMC811/Li (3.7 mAh cm⁻²), N/P = 2.7, 2.8 Ah, 437 Wh kg⁻¹	4.3 V, 0.2 C, 95.4 % after 60 cycles
High concentration electrolytes	10 M LiFSI in EC/DMC ¹⁵	not mentioned	NMC622/Li (13 mg cm ⁻²)	4.6 V, 86 % after 100 cycles
	7 M LiFSI in FEC ¹⁶	not mentioned	LNMO/Li (1.83 mAh cm ⁻²), N/P = 1.4	5 V, ~70 % after 140 cycles
	4 M LiFSI in DEE ¹⁷	8 g Ah ⁻¹	NMC811/Li (4.8 mAh cm ⁻²), N/P = 2	4.4 V, 0.2 C, 80 % after 182 cycle
Localized high concentration electrolytes	1.2 M LiFSI 0.15 M LiDFOB in EC/EMC/BTFE ¹⁸	~ 6.6 mL Ah ⁻¹	NMC111/Li (3 mAh cm ⁻²), N/P = 3.33	4.3 V, C/3, 80 % after 85 cycles
	1LiFSI-1.2DME-3TTE ¹⁹	3 g Ah ⁻¹	NMC811/Li (4.2 mAh cm ⁻²), N/P = 2.4	4.4 V, C/3, 80 % after 155 cycles
	1 M LiFSI in DME/TFE ²⁰	50 g Ah ⁻¹	NMC811/Li (1.5 mAh cm ⁻²), N/P = 6.7	4.4 V, C/3, 80 % after 300 cycles
Dual-salt electrolytes	2 M LiTFSI 2 M LiDFOB in DME ²¹	~ 40 mL Ah ⁻¹	NMC111/Li (1.7 mAh cm ⁻²), N/P = 30	4.3 V, C/3, 79 % after 500 cycles
	1 M LiTFSI 2 M LiFSI 3 wt. % LiNO ₃ in DME/DOL ²²	Not mentioned	LiFePO ₄ /Li (0.85 mAh cm ⁻²), N/P = 0.44	3.8 V, C/4, 83 % after 100 cycles
	0.6 M LiDFOB, 0.6 M LiBF ₄ in FEC: DEC 1:2 (v/v) ²³	~2.7 g Ah ⁻¹	NCM532/Cu (2.4 mAh cm ⁻²)	4.5 V, C/5, 80 % after 80 cycles
Fluorinated Solvents	1 M LiPF ₆ in FEC/FEMC/HFE ²⁴	47 g Ah ⁻¹	NMC811/Li (2 mAh cm ⁻²), N/P = 1	4.4 V, C/2, 120 cycles
	1 M LiTFSI in FDMA/FEC ²⁵	30 g Ah ⁻¹	NMC811/Li (3.5 mAh cm ⁻²), N/P = 1.5	4.3 V, 0.25C, 90 % after 100cycles
	1 M LiFSI in FDMB ²⁶	~ 6 g Ah ⁻¹	NMC532/Li (1.6 mAh cm ⁻²), N/P = 2.5	4.2 V, C/3, 100 % after 210 cycles
	1 M LiFSI in FSA ²⁷	~ 25 mL Ah ⁻¹	NMC622/Li (1.6 mAh cm ⁻²), N/P = 7.6	4.3 V, 89 % after 200 cycles
	1 M LiFSI in DMTMSA ²⁸	2.62 g Ah ⁻¹	NMC811/Li (4.86 mAh cm ⁻²), N/P = 0.39	4.7 V, 0.15 C, 88 % after 90 cycles
	1 M LiFSI in DME/FDMH ²⁹	~10 mL Ah ⁻¹	NMC811/Li (2 mAh cm ⁻²), N/P = 2	4.4 V, C/2, 76 % after 250 cycles

	1.2 M LiFSI in F5DEE ³⁰	8 g Ah ⁻¹	NMC811/Li (4.9 mAh cm ⁻²), N/P ≈ 2	4.4 V, 0.2C, 80 % after 200cycles
Additive-assisted electrolytes	1 M LiPF ₆ in EC/DEC with 10 mM In(OTf) ₃ and 0.5 M LiNO ₃ ³¹	8.37 g Ah ⁻¹	NMC811/Li (4.3 mAh cm ⁻²), N/P = 2.09	4.3 V, 0.3C 80 % after 160 cycles
	0.8 M LiTFSI 0.2 M LiDFOB 0.05 M LiPF ₆ in 3EMC/FEC with 1 wt.% P ₂ S ₅ -saturated CS ₂ ³²	4 mL Ah ⁻¹	NCMA/Li (4 mAh cm ⁻²), N/P = 5	4.3 V, 0.2C 80 % after 130 cycles
	0.8 M LiPF ₆ in FEC/DMC with 5 wt.% (4 M LiNO ₃ in DMSO) ³³	7.9 mL Ah ⁻¹	NMC811/Li (2.5 mAh cm ⁻²), N/P = 4	4.4 V, 0.5C, 75 % after 200cycles
	1 M LiPF ₆ in EC/DEC with 0.4 wt.% Al(EtO) ₃ and 5 vol.% FEC ³⁴	3.4 g Ah ⁻¹	NMC811/Li (4 mAh cm ⁻²), N/P = 2.13	4.5 V, 0.1C 80.3 % after 130 cycles

Table S2 | Electrochemical performances of representative *in-situ* polymerized gel polymer electrolytes (GPEs) for LMBs.

	Monomer	Formula	Ion transport properties (σ , T_{Li^+} , etc.)	Initiator	Type of polymerization	Cell condition	Cycling condition & capacity retention
This work	LiFPA	3D-SIPE-LiFPA	2.48 mS cm⁻¹ at 30 °C, $t_{Li^+} = 0.915$	-	Thermal	NMC811/Li (3.7 mAh cm⁻²), N/P = 2.7	4.3 V, 0.2 C, 80.8 % after 236 cycles
This work	This work Pouch cell	3D-SIPE-LiFPA	2.48 mS cm⁻¹ at 30 °C, $t_{Li^+} = 0.915$	-	Thermal	NMC811/Li (3.7 mAh cm⁻²), N/P = 2.7, 222 mAh, 300 Wh kg⁻¹	4.3 V, 0.2 C, 90.0 % after 120 cycles
This work	This work Pouch cell	3D-SIPE-LiFPA	2.48 mS cm⁻¹ at 30 °C, $t_{Li^+} = 0.915$	-	Thermal	NMC811/Li (3.7 mAh cm⁻²), N/P = 2.7, 2.8 Ah, 437 Wh kg⁻¹	4.3 V, 0.2 C, 95.4 % after 60 cycles
Ref ³⁵	PEGMEM, PEGDMA	LiTFSI, PC	0.11 mS cm ⁻¹ at 25 °C, $T_{Li^+} = 0.88$	HMPP	UV	LiFePO ₄ /Li (5 mg cm ⁻²), N/P = not mentioned	0.1 C, 100 % after 100 cycles
Ref ³⁶	VC	LiDFOB	0.022 mS cm ⁻¹ at 25 °C	AIBN	Thermal	LiCoO ₂ /Li (1.5 mg cm ⁻²), N/P = not mentioned	4.3 V, 0.1 C, 84 % after 150 cycles
Ref ³⁷	PEGDA	LiTFSI, LiBOB, and glutaronitrile	1 mS cm ⁻¹ at 30 °C	Irgacure 819	UV	LiFePO ₄ /Li (2–3.0 mg cm ⁻²), N/P = not mentioned	3.9 V, 0.2 C, 93 % after 200 cycles
Ref ³⁸	1.3-DOL	LiTFSI	1 mS cm ⁻¹ at RT	Al(OTf) ₃	-	LiFePO ₄ /Li (5 mg cm ⁻²), N/P = not mentioned	4 V, 1 C, 75 % 700 cycles
Ref ³⁹	1.3-DOL	LiTFSI	~1.8 mS cm ⁻¹ at RT	AlF ₃	-	LNCM622/Li (3 mg cm ⁻²), N/P = not mentioned	4.2 V, 0.1 C, 80 % after 50 cycles
Ref ⁴⁰	PEGDMA, PETEA	LiPF ₆ , EC, DEC, EMC	7.6 mS cm ⁻¹ at RT	AIBN	Thermal	LiFePO ₄ /Li (3 mg cm ⁻²), N/P = not mentioned	4.2 V, 0.5 C, 90 % after 240 cycles
Ref ⁴¹	VC	LiTFSI, TEP, VC	4.4 mS cm ⁻¹ at RT	AIBN	Thermal	NCM811/Li (1 mAh cm ⁻²), N/P = not mentioned	4.3 V, 0.5 C, 87 % after 200cycles
Ref ⁴²	1.3-DOL	LiTFSI, DOL, DME	3.8 mS cm ⁻¹ at RT	LiPF ₆	Thermal	NCM622/Li (3 mg cm ⁻²), N/P =	4.3 V, 0.5C, 86% after

						not mentioned	100 cycles
Ref ⁴³	1.3-DOL	LiTFSI, DOL	1.1 mS cm ⁻¹ at RT	TB	-	NCM622/Li (4 mg cm ⁻²), N/P = not mentioned	4.3 V, 0.5C, 80% after 200 cycles

Table S3 | Electrochemical performances of representative *ex-situ* solid polymer electrolytes (SPEs) for LMBs.

	Formula	Coin-cell condition	Coin-cell performance	Pouch-cell condition	Pouch-cell performance
This work	3D-SIPE-LiFPA	NMC811/Li (3.7 mAh cm⁻²), N/P = 2.7	4.3 V, 0.2 C, 80.8 % after 236 cycles	NMC811/Li (3.7 mAh cm⁻²), N/P = 2.7, 2.8 Ah, 437 Wh kg⁻¹	4.3 V, 0.2 C, 95.4 % after 60 cycles
Ref ⁴⁴	BA, SN, PEGDA, LiTFSI	NMC811/Li (2 mAh cm ⁻²), N/P = 3.4	4.3 V, 0.25 C, 88.0 % after 100 cycles	Unassembled test, theoretically energy density > 400 wh kg ⁻¹	-
Ref ⁴⁵	LiPF ₆ , ZIF-5, SiO ₂ , PVDF-HFP	NMC811/Li (1 mAh cm ⁻²), N/P > 10	4.3 V, 1 C, 90.0 % after 300 cycles	Unassembled test	-
Ref ⁴⁶	PVDF, LiTFSI, LLZTO, LiFSI, FEC, PEGMA/BEMA	LiNO ₂ /Li (0.8 mAh cm ⁻²), N/P = 4	4.4 V, 0.5 C, 81.0 % after 200 cycles	Unassembled test	-
Ref ⁴⁷	SN, FEC, LiTFSI, PEA, PEGDAM	NMC811/Li (2.3 mAh cm ⁻²), N/P = 2.3	4.3 V, 0.2 C, > 90.0 % after 60 cycles	Unassembled test	-
Ref ⁴⁸	Diglyme, LiNO ₃ , HFIP, LiBOB	NMC622/Li (2 mAh cm ⁻²), N/P = 5	4.2 V, 0.2 C, > 80.0 % after 200 cycles	Unassembled test	-
Ref ⁴⁹	Fluorinated graphene, PVDF, HFP, LiTFSI	NMC622/Li (1.1 mAh cm ⁻²), N/P = not mentioned	4.3 V, 0.2 C, 60.0 % after 60 cycles	Unassembled test	-
Ref ⁵⁰	UFF, PEO, PAN, LiTFSI	NMC811/Li (3.6 mAh cm ⁻²), N/P = 1.1	4.3 V, 0.1 C, 50 °C, 78.0 % after 100 cycles	NMC811/Li (2.3 mAh cm ⁻²), N/P = 1.7, Energy density = not mentioned	4.3 V, 2cycles
Ref ⁵¹	DOL, MP, LiTFSI, LiPF ₆ , FEC	NMC811/Li (1.4 mAh cm ⁻²), N/P = not mentioned	4.3 V, 0.1 C, 80.0 % after 100 cycles	Unassembled test	-
Ref ⁴³	LiTFSI, DOL, TB	NMC622/Li (0.7 mAh cm ⁻²), N/P = not mentioned	4.3 V, 0.5 C, 80.0 % after 200 cycles	Unassembled test	-
Ref ⁵²	BA, SN, PEGDA, LiTFSI, FEC	NMC83/Li (0.7 mAh cm ⁻²), N/P = not mentioned	4.3 V, 0.5 C, > 80.0 % after 25 cycles	Unassembled test, theoretically energy density > 400 wh kg ⁻¹	-

Table S4 | The EDS element content of dry polymer powder obtained from 3D-SIPE-LiFPA.

Element	Weight percentage (%)	Atomic percentage (%)
C	7.24	11.26
O	15.49	18.09
F	58.87	57.91
Al	18.40	12.74
	100.00	100.00

Table S5 | MD simulations.

	EMC/FEC/LiFPA or EMC/FEC/ LiPF ₆ =5/7/1
Number of EMC per box	200
Number of FEC per box	280
Number of LiFPA or LiPF ₆ per box	40
Total number of atoms	7480
Simulation box size (Å ³)	50.7×50.7×50.7
MD, density (g/cm ³)	1.270
Bias temperature (K)	303

Table S6 | Cell parameters of the pouch type NMC811/Li LMB.

	Parameter	Value
Li anode	Thickness	50 μm
	Area capacity	10 mAh cm ⁻²
Al foil	Thickness	8 μm
NCM811 cathode	Area capacity	3.7 mAh cm ⁻²
	N/P ratio	2.7
Electrolyte	E/C ratio	2.0 g Ah ⁻¹
Separator	Thickness	25 μm
Cell	Average voltage	3.8V
	Capacity	2.8 Ah
	Gravimetric energy density	437 Wh kg ⁻¹

Table S7 | ARC data comparison of different electrolytes based LMBs.

	Reference	Formula	Cell condition	Equipment types of ARC test	T _{onset}	T _{tr}
Polymer electrolytes	Our work	3D-SIPE-LiFPA	100% SOC; 2.8 Ah; NCM811/Li LMBs;	HEL	120 °C	185 °C (1 °C min ⁻¹)
	Ref ⁵³	PEO, LiTFSI	SOC not mentioned;	THT	155 °C	260 °C (0.48 °C min ⁻¹)

			0.0045 Ah; LiCoO ₂ /Li LMBs;			
	Ref ⁵⁴	PEO , LiTFSI	100% SOC; Capacity not mentioned; LiFePO ₄ /Li LMBs;	THT	247 °C	No thermal runaway
	Ref ⁴¹	PEG, CA, LLZTO, LiTFSI, LiDFOB, AIBN	100% SOC; Capacity not mentioned; LiCoO ₂ /Li LMBs;	HEL	160 °C	No thermal runaway
	Ref ⁵⁵	PEO, LiTFSI, SN, LiTFPB	100% SOC; 3 Ah; LiCoO ₂ /Li LMBs;	HEL	60 °C	Not mentioned
	Ref ⁵⁶	CUEM, AIBN, LiDFOB, EC, DMC	SOC not mentioned; Capacity Not mentioned; NCM622/Li LMBs;	HEL	Not mentio ned	210 °C (1 °C min ⁻¹)
Inorganic solid electrolytes	Ref ⁵⁷	LATP with pristine Li metal		THT	291 °C	302 °C (60 °C min ⁻¹)
	Ref ⁵⁷	LAGP with pristine Li metal		THT	262 °C	320 °C (60 °C min ⁻¹)
	Ref ⁵⁷	LLTO with pristine Li metal		THT	251 °C	256 °C (60 °C min ⁻¹)
	Ref ⁵⁷	LLZO with pristine Li metal		THT	293 °C	No thermal runaway
	Ref ⁵⁸	LPSCI with pristine Li metal		HEL	235 °C	No thermal runaway
	Ref ⁵⁸	LPSCI	100% SOC; 1.5 Ah; S/Li battery;	HEL	90 °C	190 °C (1 °C min ⁻¹)
	Ref ⁵⁹	LATP	Li/Li battery	THT	173 °C	207 °C (10 °C min ⁻¹)
	Ref ⁵⁹	BNRA- LATP	Li/Li battery	THT	194 °C	265 °C (10 °C min ⁻¹)

Supplementary References

- 1 L. Li, G. Xu, S. Zhang, S. Dong, S. Wang, Z. Cui, X. Du, C. Wang, B. Xie, J. Du, X. Zhou and G. Cui, *ACS Energy Lett.*, 2022, **7**, 591-598.
- 2 N. Piao, S. Liu, B. Zhang, X. Ji, X. Fan, L. Wang, P. F. Wang, T. Jin, S. C. Liou, H. Yang, J. Jiang, K. Xu, M. A. Schroeder, X. He and C. Wang, *ACS Energy Lett.*, 2021, **6**, 1839-1848.
- 3 K. Xu, Y. Lam, S. Zhang, T. R. Jow and T. B. Curtis, *J. Phys. Chem. C*, 2007, **111**, 7411.
- 4 H. Sun, *J. Phys. Chem. B*, 1998, **102**, 7338-7364.
- 5 A. A. Samoletov, C. P. Dettmann and M. A. Chaplain, *J. Stat. Phys.*, 2007, **128**, 1321-1336.
- 6 H. J. C. Berendsen, J. P. M. Postma, W. F. van Gunsteren, A. DiNola and J. R. Haak, *J. Chem. Phys.*, 1984, **81**, 3684-3690.
- 7 P. P. Ewald, *Ann. Phys.*, 1921, **369**, 253-287.
- 8 M. P. Tosi, in *Solid State Phys.*, Academic Press, New York, San Francisco, 1964, vol. 16, pp. 1-120.
- 9 G. Yang, R. L. Sacci, I. N. Ivanov, R. E. Ruther, K. A. Hays, Y. Zhang, P. F. Cao, G. M. Veith, N. J. Dudney, T. Saito, D. T. Hallinan and J. Nanda, *J. Electrochem. Soc.*, 2019, **166**, A178-A187.
- 10 Z. Chen, Y. Tang, X. Du, B. Chen, G. Lu, X. Han, Y. Zhang, W. Yang, P. Han, J. Zhao and G. Cui, *Angew. Chem. Int. Ed.*, 2020, **59**, 21769-21777.
- 11 X. Fan, X. Ji, L. Chen, J. Chen, T. Deng, F. Han, J. Yue, N. Piao, R. Wang, X. Zhou, X. Xiao, L. Chen and C. Wang, *Nat. Energy*, 2019, **4**, 882-890.
- 12 S. Li, L. Fan and Y. Lu, *Energy Storage Mater.*, 2019, **18**, 205-212.
- 13 Y. Wu, S. Wang, H. Li, L. Chen and F. Wu, *InfoMat*, 2021, **3**, 827-853.
- 14 S. J. Yang, N. Yao, F. N. Jiang, J. Xie, S. Y. Sun, X. Chen, H. Yuan, X. B. Cheng, J. Q. Huang and Q. Zhang, *Angew. Chem. Int. Ed.*, 2022, **61**, e202214545.
- 15 X. Fan, L. Chen, X. Ji, T. Deng, S. Hou, J. Chen, J. Zheng, F. Wang, J. Jiang, K. Xu and C. Wang, *Chem*, 2018, **4**, 174-185.
- 16 L. Suo, W. Xue, M. Gobet, S. G. Greenbaum, C. Wang, Y. Chen, W. Yang, Y. Li and J. Li, *Proc. Natl. Acad. Sci.*, 2018, **115**, 1156-1161.

- 17 Y. Chen, Z. Yu, P. Rudnicki, H. Gong, Z. Huang, S. C. Kim, J. C. Lai, X. Kong, J. Qin, Y. Cui and Z. Bao, *J. Am. Chem. Soc.*, 2021, **143**, 18703-18713.
- 18 L. Yu, S. Chen, H. Lee, L. Zhang, M. H. Engelhard, Q. Li, S. Jiao, J. Liu, W. Xu and J.-G. Zhang, *ACS Energy Lett.*, 2018, **3**, 2059-2067.
- 19 X. Ren, L. Zou, X. Cao, M. H. Engelhard, W. Liu, S. D. Burton, H. Lee, C. Niu, B. E. Matthews, Z. Zhu, C. Wang, B. W. Arey, J. Xiao, J. Liu, J.-G. Zhang and W. Xu, *Joule*, 2019, **3**, 1662-1676.
- 20 X. Cao, X. Ren, L. Zou, M. H. Engelhard, W. Huang, H. Wang, B. E. Matthews, H. Lee, C. Niu, B. W. Arey, Y. Cui, C. Wang, J. Xiao, J. Liu, W. Xu and J.-G. Zhang, *Nat. Energy*, 2019, **4**, 796-805.
- 21 S. Jiao, X. Ren, R. Cao, M. H. Engelhard, Y. Liu, D. Hu, D. Mei, J. Zheng, W. Zhao, Q. Li, N. Liu, B. D. Adams, C. Ma, J. Liu, J. G. Zhang and W. Xu, *Nat. Energy*, 2018, **3**, 739-746.
- 22 F. Qiu, X. Li, H. Deng, D. Wang, X. Mu, P. He and H. Zhou, *Adv. Energy Mater.*, 2018, **9**, 1803372.
- 23 R. Weber, M. Genovese, A. J. Louli, S. Hames, C. Martin, I. G. Hill and J. R. Dahn, *Nat. Energy*, 2019, **4**, 683-689.
- 24 X. Fan, L. Chen, O. Borodin, X. Ji, J. Chen, S. Hou, T. Deng, J. Zheng, C. Yang, S. C. Liou, K. Amine, K. Xu and C. Wang, *Nat. Nanotechnol.*, 2018, **13**, 715-722.
- 25 Q. Wang, Z. Yao, C. Zhao, T. Verhallen, D. P. Tabor, M. Liu, F. Ooms, F. Kang, A. Aspuru-Guzik, Y. S. Hu, M. Wagemaker and B. Li, *Nat. Commun.*, 2020, **11**, 4188.
- 26 Z. Yu, H. Wang, X. Kong, W. Huang, Y. Tsao, D. G. Mackanic, K. Wang, X. Wang, W. Huang, S. Choudhury, Y. Zheng, C. V. Amanchukwu, S. T. Hung, Y. Ma, E. G. Lomeli, J. Qin, Y. Cui and Z. Bao, *Nat. Energy*, 2020, **5**, 526-533.
- 27 W. Xue, Z. Shi, M. Huang, S. Feng, C. Wang, F. Wang, J. Lopez, B. Qiao, G. Xu, W. Zhang, Y. Dong, R. Gao, Y. Shao-Horn, J. A. Johnson and J. Li, *Energy Environ. Sci.*, 2020, **13**, 212-220.
- 28 W. Xue, M. Huang, Y. Li, Y. G. Zhu, R. Gao, X. Xiao, W. Zhang, S. Li, G. Xu, Y. Yu, P. Li, J. Lopez, D. Yu, Y. Dong, W. Fan, Z. Shi, R. Xiong, C. J. Sun, I. Hwang, W. K. Lee, Y. Shao-Horn, J. A. Johnson and J. Li, *Nat. Energy*, 2021, **6**, 495-505.

- 29 H. Wang, Z. Yu, X. Kong, W. Huang, Z. Zhang, D. G. Mackanic, X. Huang, J. Qin, Z. Bao and Y. Cui, *Adv. Mater.*, 2021, **33**, 2008619.
- 30 Z. Yu, P. E. Rudnicki, Z. Zhang, Z. Huang, H. Celik, S. T. Oyakhire, Y. Chen, X. Kong, S. C. Kim, X. Xiao, H. Wang, Y. Zheng, G. A. Kamat, M. S. Kim, S. F. Bent, J. Qin, Y. Cui and Z. Bao, *Nat. Energy*, 2022, **7**, 94-106.
- 31 W. Zhang, Z. Shen, S. Li, L. Fan, X. Wang, F. Chen, X. Zang, T. Wu, F. Ma and Y. Lu, *Adv. Funct. Mater.*, 2020, **30**, 2003800.
- 32 S. H. Lee, J. Y. Hwang, J. Ming, H. Kim, H. G. Jung and Y. K. Sun, *ACS Energy Lett.*, 2021, **6**, 2153-2161.
- 33 S. Liu, X. Ji, N. Piao, J. Chen, N. Eidson, J. Xu, P. Wang, L. Chen, J. Zhang, T. Deng, S. Hou, T. Jin, H. Wan, J. Li, J. Tu and C. Wang, *Angew. Chem. Int. Ed.*, 2021, **60**, 3661-3671.
- 34 Y. Zhang, Y. Wu, H. Li, J. Chen, D. Lei and C. Wang, *Nat. Commun.*, 2022, **13**, 1-13.
- 35 L. Porcarelli, A. S. Shaplov, F. Bella, J. R. Nair, D. Mecerreyes and C. Gerbaldi, *ACS Energy Lett.*, 2016, **1**, 678-682.
- 36 J. Chai, Z. Liu, J. Ma, J. Wang, X. Liu, H. Liu, J. Zhang, G. Cui and L. Chen, *Adv. Sci.*, 2017, **4**, 1600377.
- 37 S. Li, Y.-M. Chen, W. Liang, Y. Shao, K. Liu, Z. Nikolov and Y. Zhu, *Joule*, 2018, **2**, 1838-1856.
- 38 Q. Zhao, X. Liu, S. Stalin, K. Khan and L. A. Archer, *Nat. Energy*, 2019, **4**, 365-373.
- 39 C. Z. Zhao, Q. Zhao, X. Liu, J. Zheng, S. Stalin, Q. Zhang and L. A. Archer, *Adv. Mater.*, 2020, **32**, 1905629.
- 40 Q. Wang, X. Xu, B. Hong, M. Bai, J. Li, Z. Zhang and Y. Lai, *Chem. Eng. J.*, 2022, **428**.
- 41 S. J. Tan, J. Yue, Y. F. Tian, Q. Ma, J. Wan, Y. Xiao, J. Zhang, Y. X. Yin, R. Wen, S. Xin and Y. G. Guo, *Energy Storage Mater.*, 2021, **39**, 186-193.
- 42 F. Q. Liu, W. P. Wang, Y. X. Yin, S. F. Zhang, J. L. Shi, L. Wang, X. D. Zhang, Y. Zheng, J. J. Zhou, L. Li and Y. G. Guo, *Sci. Adv.*, 2018, **4**, eaat5383
- 43 J. Xiang, Y. Zhang, B. Zhang, L. Yuan, X. Liu, Z. Cheng, Y. Yang, X. Zhang, Z. Li, Y. Shen, J. Jiang and Y. Huang, *Energy Environ. Sci.*, 2021, **14**, 3510-3521.

- 44 M. J. Lee, J. Han, K. Lee, Y. J. Lee, B. G. Kim, K. N. Jung, B. J. Kim and S. W. Lee, *Nature*, 2022, **601**, 217-222.
- 45 H. X. Yang, Z. K. Liu, Y. Wang, N. W. Li and L. Yu, *Adv. Funct. Mater.*, 2022, DOI: 10.1002/adfm.202209837, 2209837.
- 46 T. Deng, L. Cao, X. He, A. M. Li, D. Li, J. Xu, S. Liu, P. Bai, T. Jin, L. Ma, M. A. Schroeder, X. Fan and C. Wang, *Chem*, 2021, **7**, 3052-3068.
- 47 R. Lin, Y. He, C. Wang, P. Zou, E. Hu, X. Q. Yang, K. Xu and H. L. Xin, *Nat. Nanotechnol.*, 2022, **17**, 768-776.
- 48 S. Choudhury, Z. Tu, A. Nijamudheen, M. J. Zachman, S. Stalin, Y. Deng, Q. Zhao, D. Vu, L. F. Kourkoutis, J. L. Mendoza-Cortes and L. A. Archer, *Nat. Commun.*, 2019, **10**, 3091.
- 49 P. Zhai, Z. Yang, Y. Wei, X. Guo and Y. Gong, *Adv. Energy Mater.*, 2022, **12**, 2200967.
- 50 F. He, W. Tang, X. Zhang, L. Deng and J. Luo, *Adv. Mater.*, 2021, **33**, 2105329.
- 51 J. Yu, X. Lin, J. Liu, T. T. Yu, M. J. Robson, G. Zhou, H. M. Law, H. Wang, B. Z. Tang and F. Ciucci, *Adv. Energy Mater.*, 2021, **12**, 2102932.
- 52 J. Han, M. J. Lee, K. Lee, Y. J. Lee, S. H. Kwon, J. H. Min, E. Lee, W. Lee, S. W. Lee and B. J. Kim, *Adv. Mater.*, 2022, DOI: 10.1002/adma.202205194, 2205194.
- 53 J. Lu, J. Zhou, R. Chen, F. Fang, K. Nie, W. Qi, J. N. Zhang, R. Yang, X. Yu, H. Li, L. Chen and X. Huang, *Energy Storage Mater.*, 2020, **32**, 191-198.
- 54 A. Perea, M. Dontigny and K. Zaghib, *J. Power Sources*, 2017, **359**, 182-185.
- 55 C. Wang, T. Wang, L. Wang, Z. Hu, Z. Cui, J. Li, S. Dong, X. Zhou and G. Cui, *Adv. Sci.*, 2019, **6**, 1901036.
- 56 H. Xu, C. Sun, S. Zhang, H. Zhang, Z. Liu, Y. Tang and G. Cui, *ChemSusChem*, 2023, DOI: 10.1002/cssc.202202334, e202202334.
- 57 R. Chen, A. M. Nolan, J. Lu, J. Wang, X. Yu, Y. Mo, L. Chen, X. Huang and H. Li, *Joule*, 2020, **4**, 812-821.
- 58 L. Huang, T. Lu, G. Xu, X. Zhang, Z. Jiang, Z. Zhang, Y. Wang, P. Han, G. Cui and L. Chen, *Joule*, 2022, **6**, 906-922.

59 L. Zhu, Y. Wang, Y. Wu, W. Feng, Z. Liu, W. Tang, X. Wang and Y. Xia, *Adv. Funct. Mater.*, 2022, **32**, 2201136.